



香港城市大學
City University of Hong Kong

專業 創新 胸懷全球
Professional · Creative
For The World

CityU Scholars

Copper-alumina Hybrid Nanofluid Droplet Phase Change Dynamics over Heated Plain Copper and Porous Residue Surfaces

Siddiqui, F. R.; Tso, C. Y.; Qiu, H. H.; Chao, Christopher Y. H.; Fu, S. C.

Published in:

International Journal of Thermal Sciences

Published: 01/12/2022

Document Version:

Post-print, also known as Accepted Author Manuscript, Peer-reviewed or Author Final version

License:

CC BY-NC-ND

Publication record in CityU Scholars:

[Go to record](#)

Published version (DOI):

[10.1016/j.ijthermalsci.2022.107795](https://doi.org/10.1016/j.ijthermalsci.2022.107795)

Publication details:

Siddiqui, F. R., Tso, C. Y., Qiu, H. H., Chao, C. Y. H., & Fu, S. C. (2022). Copper-alumina Hybrid Nanofluid Droplet Phase Change Dynamics over Heated Plain Copper and Porous Residue Surfaces. *International Journal of Thermal Sciences*, 182, Article 107795. <https://doi.org/10.1016/j.ijthermalsci.2022.107795>

Citing this paper

Please note that where the full-text provided on CityU Scholars is the Post-print version (also known as Accepted Author Manuscript, Peer-reviewed or Author Final version), it may differ from the Final Published version. When citing, ensure that you check and use the publisher's definitive version for pagination and other details.

General rights

Copyright for the publications made accessible via the CityU Scholars portal is retained by the author(s) and/or other copyright owners and it is a condition of accessing these publications that users recognise and abide by the legal requirements associated with these rights. Users may not further distribute the material or use it for any profit-making activity or commercial gain.

Publisher permission

Permission for previously published items are in accordance with publisher's copyright policies sourced from the SHERPA RoMEO database. Links to full text versions (either Published or Post-print) are only available if corresponding publishers allow open access.

Take down policy

Contact lbscholars@cityu.edu.hk if you believe that this document breaches copyright and provide us with details. We will remove access to the work immediately and investigate your claim.

© 2022. This manuscript version is made available under the CC-BY-NC-ND 4.0 license <https://creativecommons.org/licenses/by-nc-nd/4.0/>.

1 **Copper-alumina hybrid nanofluid droplet phase change dynamics over heated plain**
2 **copper and porous residue surfaces**

3
4 F.R. Siddiqui¹, C.Y. Tso², H.H. Qiu¹, Christopher Y. H. Chao³, S.C. Fu^{4*}
5

6 ¹Department of Mechanical and Aerospace Engineering, The Hong Kong University of Science
7 and Technology, Hong Kong

8 ²School of Energy and Environment, City University of Hong Kong, Hong Kong

9 ³Department of Building Environment and Energy Engineering, Department of Mechanical
10 Engineering, The Hong Kong Polytechnic University, Hong Kong

11 ⁴Department of Mechanical Engineering, The University of Hong Kong, Hong Kong

12 *Corresponding Author Tel.: +852 3910 2154

13 E-mail Address: scfu@hku.hk

14 Postal Address: Department of Mechanical Engineering, The University of Hong Kong, Pokfulam
15 Road, Hong Kong
16

17 **Abstract**

18 Droplet phase change is the key phenomenon for high heat transfer rates in spray or drop-wise
19 cooling applications. Despite high cooling efficiency of the spray cooling technology,
20 conventional fluids, such as water, cannot be used for thermal management of modern high heat
21 flux devices due to their immense power density, resulting in early device failures. To address this
22 issue, in this research, we experimentally study the evaporation performance for various volumes
23 of the copper-alumina hybrid nanofluid (CAHF) droplet on a plain copper substrate and compare
24 it with water (H₂O) droplet in sub-boiling and boiling regimes (i.e., for substrate temperatures of
25 25-170 °C). We also numerically investigate and compare the internal velocity and thermal fields
26 of CAHF and H₂O droplets on a heated plain copper substrate. Besides the plain copper surface,
27 we examine the phase change behaviour of the subsequent CAHF droplet over a heated residue
28 surface that was obtained from the phase transition of the first CAHF droplet on a heated plain
29 copper substrate. Our results demonstrate that the evaporation rate of CAHF droplets on a plain
30 copper surface is up to 24% and an order of magnitude higher than water droplets in sub-boiling
31 and nucleate boiling regimes, respectively. Moreover, the evaporation rate of the CAHF droplet

32 on a residue surface increases up to 141% and 800% compared to that on a plain copper surface in
33 sub-boiling and nucleate boiling regimes, respectively. Furthermore, the latent heat flux up to 10
34 times can be achieved using the CAHF droplet compared to H₂O droplet on a plain copper substrate
35 in the nucleate boiling region, making the CAHF a potential fluid for high heat flux cooling
36 applications.

37

38 *Keywords:* Hybrid nanofluid, droplet phase change, heated residue, latent heat flux, Marangoni
39 convection.

40

41 **1. Introduction**

42 Cooling technologies based on droplet evaporation, for instance spray cooling, offer much higher
43 heat rejection rates than single-phase heat transfer processes. However, in recent years, heat
44 generation in high heat flux devices has reached unprecedented levels ($>100 \text{ W/cm}^2$) that cannot
45 be thermally managed by existing thermal fluids due to their lower heat rejection capacity. This
46 not only resulted in early device failures, but also inhibited the future growth of high heat
47 dissipating devices, prompting a need to investigate advanced heat transfer fluids with high heat
48 rejection capability. Such advanced fluids when used in efficient cooling technologies, for example
49 spray cooling, may resolve thermal management issues in high heat flux applications.
50 Conventional fluids, for instance water, can be transformed into highly efficient heat transfer fluids
51 by adding a small fraction of nanometer-sized particles, known as nanofluids.

52

53 Nanofluids show a higher thermal conductivity than their respective base fluids due to the
54 dispersed nanoparticles [1–5]. The nanofluid thermal characteristics depends on several factors,
55 such as temperature, dispersion stability, base fluid and nanoparticle type, size, shape and
56 concentration [6–8]. Although nanofluids possess advanced thermal characteristics due to high
57 thermal conductivity, they do not exhibit all the necessary (rheological and thermal) properties
58 needed in heat transfer applications [9]. For example, metal-oxide nanofluids exhibit higher
59 dispersion stability but lower thermal conductivity than metal nanofluids. Conversely, metal
60 nanofluids possess high thermal conductivity and exhibit poor dispersion stability. As nanofluids
61 do not possess all essential characteristics needed in heat transfer fluids, they cannot be used in
62 their current form for effective cooling of high heat flux devices [10].

63

64 More recently, an advanced form of nanofluid was investigated with much better dispersion
65 stability and thermal conductivity than single particle nanofluid and was named hybrid nanofluid
66 [11–13]. Hybrid nanofluid is prepared by dispersing any two types of nanoparticles (from metal,
67 non-metal or metal-oxide) in the base fluid. The advanced hydrodynamic and thermal properties
68 of hybrid nanofluids mainly depend on their inter-particle compatibility [14]. The thermo-
69 rheological characteristics of hybrid nanofluids comprising non-compatible nanoparticles are even
70 worse than for single particle nanofluids. Moreover, the synergy between two compatible
71 nanoparticle types leads to much higher thermal conductivity in hybrid nanofluids than single
72 particle nanofluids [15–17]. The advanced thermo-rheological properties as well as inter-particle
73 synergy in hybrid nanofluids are some of the desirable characteristics needed for high heat flux
74 device cooling.

75

76 The hybrid nanofluid, as an emerging heat transfer fluid, has not yet received sufficient attention
77 regarding its application in droplet evaporation or boiling based cooling processes. With inter-
78 particle synergy and advanced thermo-rheological properties, hybrid nanofluid droplets may
79 exhibit better heat removal rates compared to base fluid or single particle nanofluid droplets.
80 Although droplet phase change on un-heated substrates has been widely studied for single particle
81 nanofluids with a very limited focus on hybrid nanofluids [18–23], the hybrid nanofluid droplet
82 phase change on heated surfaces received no attention to date by the research community.
83 However, some researchers have studied the evaporation behaviour of single particle nanofluid
84 droplets on heated surfaces. Research indicates higher evaporation rates for single particle
85 nanofluid droplets compared to water droplets on heated substrates [24,25]. Al-Sharafi et al. [26]
86 concluded that Marangoni forces dominate buoyancy forces in the CNT based nanofluid droplet
87 on a heated substrate. In another study [27], they suggested that both Marangoni and buoyancy
88 forces contribute to circulating vortices inside the CNT nanofluid droplet during its evaporation
89 on a heated substrate.

90

91 Like evaporation, the hybrid nanofluid droplet boiling over heated surfaces was not previously
92 investigated. However, some researchers have studied the boiling behaviour of single particle
93 nanofluid droplets. Okawa et al. [28] reported significant enhancements in critical heat flux of

94 TiO₂ nanofluid droplets compared to water droplets. Duursma et al. [29] reported 10% increase in
95 heat flux of aluminium-dimethyl sulfoxide (DMSO) nanofluid droplet at 0.1% volume fraction
96 compared to the pure DMSO droplet. Paul et al. [30] showed that TiO₂ nanofluid droplets exhibit
97 much reduced evaporation time compared to water droplets at a surface temperature of 300 °C.
98 They concluded that nanofluid droplets with high particle concentration do not show the
99 Leidenfrost effect, and that these droplets release small droplets due to thermal agitation, resulting
100 in higher evaporation rates than water droplets. The literature indicates that single particle
101 nanofluids show enhanced heat flux and better droplet evaporation rates than their respective base
102 fluids, however, they are not suitable for practical applications, as they do not exhibit overall
103 thermo-rheological characteristics. Therefore, the phase change behaviour of hybrid nanofluid
104 droplets should be investigated due to their better thermo-rheological properties than single
105 particle nanofluids.

106

107 We recently showed [9] that copper-alumina hybrid nanofluid (CAHF) possesses better thermo-
108 rheological properties (high dispersion stability and enhanced thermal conductivity) than
109 corresponding single particle nanofluids (i.e., copper and alumina nanofluids) and therefore,
110 CAHF may be a suitable candidate for droplet based cooling applications. As water is one of the
111 most commonly used heat transfer fluids in high heat flux cooling applications, the key objective
112 of this paper is to investigate and compare the evaporation and boiling performances of CAHF and
113 water droplets for various droplet volumes on a plain heated copper substrate. In this paper, as
114 higher evaporation rate is achieved for CAHF droplets compared to water droplets on a plain
115 heated copper substrate, we numerically investigated and compared the internal velocity and
116 temperature fields of evaporating CAHF and H₂O droplets. Furthermore, as a novelty, we studied
117 the hybrid nanoparticle dynamics inside the CAHF droplet and compared its velocity field with
118 the flow field of surrounding fluid molecules in the CAHF droplet. We also demonstrated the
119 effects of the thermal Marangoni convection on internal velocity and thermal fields of the CAHF
120 droplet that eventually improves its evaporation rate compared to H₂O droplet. Moreover, we
121 compared the boiling dynamics of CAHF and H₂O droplets in the nucleate boiling region using a
122 high speed imaging technique. We also determined the droplet latent heat flux to assess the heat
123 removal capability of CAHF droplets in comparison to H₂O droplets for potential application of
124 the CAHF in high heat flux device cooling. We lately investigated the evaporation and boiling

125 behaviour for silver graphene hybrid nanofluid droplet with respect to mixing ratios [31], however,
126 our main focus in current study is to investigate the main differences and mechanisms involved in
127 higher evaporation rates of CAHF droplets compared to H₂O droplets.

128
129 As the CAHF droplet phase change results in a porous residue formation over a heated copper
130 surface, the effect of the heated residue surface on phase change behaviour of the subsequent
131 CAHF droplet was also investigated. The residue effect is important to consider in hybrid
132 nanofluid spray or drop-wise cooling applications, where residues from hybrid nanofluid droplet
133 phase change over a heated substrate may affect the evaporation performance of subsequent
134 incoming hybrid nanofluid droplets residing over such heated residue surfaces. Droplet residues
135 were extensively studied in the past for different forms and patterns [32–35], however, the effect
136 of heated residues on evaporation rate of following droplets has not been previously investigated.
137 Although we recently investigated the residue effect on wetting and evaporation behaviour of
138 following incoming hybrid nanofluid droplets [22,36], these studies were based on un-heated
139 residue surfaces, where the hybrid nanofluid droplet evaporation was studied at room temperature.
140 However, in the current research, we investigate the heated residue effect on phase change
141 behaviour of the subsequent CAHF droplet. The main objectives of this research can be
142 summarized as:

- 143
- 144 • To investigate and compare the evaporation and boiling performances of CAHF and
145 water droplets for various droplet volumes on a heated copper substrate.
 - 146 • To study and compare the internal velocity and temperature fields of CAHF and H₂O
147 droplets for copper surface temperatures up to $T_s = 100$ °C.
 - 148 • To examine the effect of a heated residue surface on phase change behaviour of the
149 subsequent CAHF droplet in comparison to a plain heated copper surface.
- 150

151 **2. Experimental test facility**

152 The copper-alumina hybrid nanofluid (CAHF) was prepared by dispersing copper (particle size of
153 25 nm) and alumina nanoparticles (particle size of 13 nm) in the de-ionized water followed by
154 ultrasonication using an ultrasonic bath (Model 2510, Branson, USA) for 0.5 hours [7]. As large
155 sized nanoparticles can sediment faster than small nanoparticles resulting in reduced dispersion

156 stability and low thermal conductivity, small sized copper and alumina nanoparticles were selected
157 in current research. The CAHF was prepared for a fixed mixing ratio of 0.5(Cu):0.5(Al_2O_3), as it
158 exhibits better hydro-thermal characteristics (improved dispersion stability and high thermal
159 conductivity) than other mixing ratios, as reported in our recent research [9]. Moreover, as hybrid
160 nanofluids show enhanced thermal properties at very low particle concentration, the CAHF was
161 synthesized at a low volume fraction of 0.1%. To investigate CAHF thermal conductivity
162 enhancement in comparison to de-ionized water, the thermal conductivity of CAHF and H_2O
163 samples was measured at different temperatures using a thermal conductivity analyser setup (TPS
164 500S, Hot Disk, Sweden). The detailed experimental setup for CAHF thermal conductivity
165 measurements is demonstrated in our recent study [9]. The surface tension (used in numerical
166 modelling and to determine Marangoni and dynamic Bond numbers) at various temperatures was
167 subsequently measured by using 5 μl volume of H_2O and CAHF pendant droplets at 1.4 frames
168 per second and time duration of 20 seconds in a contact angle meter (Theta, Biolin Scientific,
169 Finland). Each measurement was performed three times to reduce uncertainties in results. Later,
170 the surface tension gradient was obtained by processing measured surface tension data against
171 different temperatures. The surface tension gradient was implemented as an input parameter to
172 incorporate the effect of thermal Marangoni convection in our model.

173
174 Following the thermal conductivity and surface tension measurements, the droplet phase change
175 experiments were conducted in an environmental test chamber, where the relative humidity (RH)
176 and ambient temperature (T_a) were fixed at $RH = 0.3 \pm 0.03$ and $T_a = 25 \pm 0.3$ °C, respectively.
177 The schematic of the experimental setup used to study the evaporation of CAHF and H_2O droplets
178 on a heated copper substrate is illustrated in Fig. 1 (a). A 0.1 m x 0.15 m silicone heater mat (RS,
179 UK) with a power of 100 W was used to heat the base of a 0.05 m x 0.06 m copper plate, while
180 the copper plate surface temperature was measured using two T-type thermocouples (RS, UK).
181 Each thermocouple was placed near the opposite ends of a copper surface. A Teflon strip, screwed
182 at both ends, was used to fix each thermocouple on a copper surface such that the thermocouple
183 was sandwiched between the Teflon strip and a copper surface, as illustrated in Fig. 1 (a). The air
184 gap between the Teflon strip and the copper surface was filled with silicone thermal grease (RS,
185 UK). To ensure better thermal contact, the thermal grease was also applied between the heater and
186 the copper base. The temperature of the copper surface was increased from room temperature (25

187 °C) up to 170 °C by connecting the heater to an adjustable AC power supply. The droplet
188 evaporation process was recorded at 30 frames per second (fps) using a video camera. In the
189 nucleate boiling region, the boiling dynamics of CAHF and H₂O droplets was investigated using
190 a high speed camera (HG-100K, Redlake, USA) at frame rates ranging between 60 fps and 500
191 fps. Moreover, the droplet surface temperature during the evaporation process was measured using
192 an infrared camera (Ti25, Fluke, US). The infrared camera was calibrated using a T-type
193 thermocouple by measuring the surface temperature of water and CAHF samples in a 10 ml glass
194 beaker at every 5 °C increment in a temperature range of 30-50 °C. The maximum error between
195 the thermocouple and IR camera was 1.3 °C and 1.8 °C for the CAHF and water samples,
196 respectively, at an emissivity of 0.98. This error increased at other values of emissivity.

197
198 A micropipette was used to carefully dispense the first CAHF droplet of known droplet volumes
199 of $V_{fd} = 3, 15, 30$ and $60 \mu\text{l}$ over a plain copper substrate at a pre-set surface temperature. The
200 droplet evaporation time was determined from a video camera recording for entire droplet phase
201 change process. The droplet evaporation rate was obtained by dividing the known initial droplet
202 volume by net droplet evaporation time. As the first CAHF droplet evaporated ($V_{fd} = 3, 15, 30$ and
203 $60 \mu\text{l}$), a residue surface was formed corresponding to each droplet volume from the first CAHF
204 droplet of $V_{fd} = 3, 15, 30$ and $60 \mu\text{l}$. Subsequently, second CAHF droplet of fixed droplet volume
205 as $V_{sd} = 3 \mu\text{l}$ was dispensed over each residue surface obtained from first droplet volumes of $V_{fd} =$
206 $3, 15, 30$ and $60 \mu\text{l}$. As a result, four different droplet volume ratios were obtained as $V_{fd}/V_{sd} =$
207 $3\mu\text{l}/3\mu\text{l}=1, 15\mu\text{l}/3\mu\text{l}=5, 30\mu\text{l}/3\mu\text{l}=10$ and $60\mu\text{l}/3\mu\text{l}=20$.

208 These experiments were conducted three times to reduce measurement uncertainties. Moreover,
209 as the evaporation rate of a $3 \mu\text{l}$ CAHF droplet on its residue surface for the droplet volume ratio
210 of $V_{fd}/V_{sd} = 1$ was similar to that obtained on a plain copper surface, the results are only presented
211 for droplet volume ratios of $V_{fd}/V_{sd} = 5, 10$ and 20 in results and discussion section (Section 4).
212 Furthermore, as the same copper surface is used for both CAHF and H₂O droplets, the copper
213 surface characteristics may equally affect the evaporation rates for CAHF and H₂O droplets.

214

215 3. CAHF droplet simulation

216 The internal velocity and thermal field distribution for heated CAHF and H₂O droplets were
217 investigated by developing a numerical model using COMSOL Multiphysics. As the suspended

218 copper-alumina hybrid nanoparticles are difficult to visualize even using experimental techniques,
219 such as particle image velocimetry (PIV), we developed a numerical model to investigate the
220 hybrid nanoparticle trajectory and compare the internal velocity and temperature fields between
221 CAHF and H₂O droplets. The droplet model was built using a non-isothermal flow interface that
222 couples the flow and heat transfer interfaces within the droplet. Due to the symmetry of considered
223 sessile droplets along the vertical axis, a two dimensional axisymmetric geometry was developed
224 from an original droplet image at different time instants during the droplet evaporation using
225 ImageJ software. Furthermore, a laminar flow condition was used inside the droplet domain due
226 to extremely low Rayleigh number ($< 10^{-3}$) for studied substrate temperatures of 60-100 °C.

227
228 The CAHF thermophysical properties were defined using well-developed theoretical models for
229 hybrid nanofluids [9,11]. As the main objective of our model was to investigate the internal flow
230 and temperature fields at instantaneous steady-state points during droplet evaporation, the transient
231 evaporation effects were neglected at the droplet-air interface. However, we considered the
232 realistic boundary conditions at different time instants during the droplet evaporation by using our
233 experimental data in the model. The temperature at the droplet-solid interface was obtained from
234 the measured copper surface temperature, while the temperature at the droplet-air interface was
235 obtained using the infrared imaging temperature data (as discussed in the supplementary material).
236 In this way, the variation in droplet shape as well as boundary conditions at the droplet-air interface
237 for different time instants during the droplet evaporation process were reproduced in our model.
238 Furthermore, the slip and no-slip boundary conditions were used at droplet-air and droplet-solid
239 interfaces, respectively. Although no-slip boundary condition at droplet-solid interface does not
240 much affect the internal convection in a heated CAHF droplet, it is still considered in our model
241 since the flow velocity at droplet-solid interface must be equal to zero. Due to the high surface
242 tension gradient for CAHF and H₂O droplets (as illustrated in Fig. 2 (a)), the thermal Marangoni
243 effect along with buoyancy effect were also considered in our model. The surface tension gradient
244 was used as an input parameter to solve thermal Marangoni convection in our model. The
245 Marangoni effect was implemented in our model using the Marangoni Effect Multiphysics
246 coupling. This coupling considers the Marangoni induced flow along the droplet-air interface that
247 results from the temperature difference between the droplet three phase contact line and droplet
248 apex. On the other hand, the buoyancy effect was implemented in our model by considering the

249 Boussinesq approximation in the Navier-Stokes equation. The Boussinesq approximation accounts
 250 for buoyancy induced flow that results due to the fluid density difference between the droplet-solid
 251 interface (due to the heated surface) and droplet apex. Moreover, in our model, the Navier-Stokes
 252 equation was solved using the laminar flow interface given as:

$$\rho(V \cdot \nabla V) = -\nabla p + \nabla \cdot \left(\mu(\nabla V + (\nabla V)^T) - \frac{2}{3} \mu(\nabla \cdot V) \right) + \rho g \quad (1)$$

253 where p is the pressure and μ is the dynamic viscosity of the SGHF. Moreover, the energy equation
 254 in our model was solved using the heat transfer in fluids interface, as given by following equation:

$$\rho C_p V \cdot \nabla T = \nabla \cdot (k \nabla T) + Q + Q_p + Q_{vd} \quad (2)$$

255 where C_p is the specific heat capacity, k is the thermal conductivity of the considered SGHF, and
 256 Q , Q_p and Q_{vd} are the energy generation, pressure and viscous dissipation terms, respectively. The
 257 viscosity of hybrid nanofluids depends on nanoparticle concentration and can be estimated as [37]:
 258
 259

$$\mu_{hnf} = (1 + 2.5\phi + 6.2\phi^2)\mu_{bf} \quad (3)$$

260
 261 Where ϕ is the volume fraction of hybrid nanoparticles and μ_{bf} is the kinematic viscosity of base
 262 fluid (water). We used equation (3) to set viscosity of hybrid nanofluids as an input parameter in
 263 our model. As increased concentration (or volume fraction, ϕ) of hybrid nanoparticles during
 264 CAHF droplet evaporation increases its viscosity, the viscosity variation for different time instants
 265 of CAHF droplet evaporation was considered in our model. Moreover, the variation in hybrid
 266 nanoparticle concentration (ϕ) was determined from the variation in droplet volume (using IR
 267 imaging data) during evaporation that was used in equation (3) to determine the CAHF droplet
 268 viscosity. The dynamics of suspended hybrid nanoparticles inside the CAHF droplet was simulated
 269 using the particle tracing module. The drag, lift, gravity and thermophoretic forces that affect the
 270 hybrid nanoparticle trajectory were all included in our model. However, the Brownian force was
 271 neglected in our study, as it had a negligible effect on studied hybrid nanoparticle velocity field.
 272 This is because thermophoretic forces may have a more dominant effect on studied hybrid
 273 nanoparticle dynamics due to temperature gradient effects inside the CAHF droplet compared to
 274 Brownian forces. Some other researchers also reported the significant effect of thermophoresis up
 275 to two orders of magnitude compared to the Brownian diffusion in heated systems [38,39].
 276 Moreover, the Brownian force significantly increased the computational time of our numerical
 277 modelling. The free triangular mesh was used due to simple two dimensional axisymmetric

278 geometry of considered droplets. In order to develop a computationally inexpensive model, the
279 mesh independence study was conducted for a droplet volume of 3 μ l, as shown in Fig. 1 (b). It is
280 noticed that increasing the mesh elements from 881 to 6139 considerably affects the internal
281 velocity magnitude along the normalized droplet height. However, further increasing the mesh
282 elements does not considerably affect the velocity profile. Therefore, we used 6139 mesh elements
283 comprising extra-fine mesh at droplet boundaries and finer mesh in other areas of the droplet
284 domain.

285

286 **3.1. Model Validation**

287 We validated our water droplet numerical model using the particle image velocimetry (PIV) data
288 for heated water droplets presented by Karlsson et al. [40], as demonstrated in Fig. 1 (c). From
289 contact radius and droplet height data [40], the two dimensional droplet model was developed
290 using spherical cap equations. The spherical cap assumption was used for a reason that the contact
291 radius did not exceed the capillary length for the water droplet examined by Karlsson et al. [40].
292 During the model validation, both Marangoni and buoyancy effects were considered. The no-slip
293 and slip boundary conditions were used at droplet base and the droplet-air interface, respectively.
294 In Fig. 1 (c), it is noticeable that our model satisfactorily estimates the velocity profile along the
295 droplet height for droplet evaporation time of $t = 1-15$ s at surface temperatures of 313.15 K and
296 323. 15 K. However, small differences between the estimated and PIV results may be due to the
297 simplified assumptions in our model, such as neglecting convection currents around the droplet-
298 air interface or ignoring mass diffusion from droplet surface into the air.

299

300 **4. Results and discussion**

301 **4.1. Evaporation performance of CAHF droplets compared to H₂O droplets**

302 The evaporation rate for different substrate temperatures and droplet volumes of CAHF and H₂O
303 droplets is shown in Fig. 2 (a). A significant increase in droplet evaporation rate can be observed
304 with increasing droplet volume and copper surface temperature. The CAHF droplet evaporation
305 rate increases up to 235% on a heated copper surface with increasing droplet volume in a range
306 between 3 μ l and 60 μ l. This is for a reason that the droplet-solid and droplet-air interfacial areas
307 increase with increasing droplet volume. Large droplet contact area results in high heat transfer
308 rates between the droplet and the substrate, while large droplet-air interface area increases the mass

309 transfer from droplet surface into the surrounding air. Due to this reason, the net evaporation rate
 310 tremendously increases with increasing droplet volume. Furthermore, the CAHF droplet
 311 evaporation rate increases up to 24% compared to H₂O droplet on a heated copper surface for
 312 temperatures between 25 °C and 100 °C, as shown in Fig. 2 (a). The higher evaporation rate for
 313 the CAHF droplet over a heated copper surface is possibly due to its higher thermal conductivity
 314 than H₂O droplet (discussed in Section 4.1.1). Moreover, the suspended hybrid nanoparticles in
 315 the CAHF droplet may also modify the internal flow and temperature fields (discussed in Section
 316 4.1.1), thus resulting in higher evaporation rates than H₂O droplets. The evaporation rate for both
 317 CAHF and H₂O droplets on copper substrate can be estimated from the following empirical
 318 equation:

$$E = aE_o \left(\frac{T_s}{T_b} \right)^b \quad (4)$$

321
 322 where T_b is the droplet temperature at its boiling point ($T_s = 100$ °C), E_o is the evaporation rate of
 323 smallest considered droplet volume ($V_o = 3$ μl) over a copper substrate at room temperature of 25
 324 °C, the coefficient $a = C_1(V/V_o)^{C_2}$ and constant $b = 3$. V is any droplet volume in a range of 3-60
 325 μl, constants C_1 and C_2 are equal to 67.318 and 0.386 for CAHF droplets while these are equal to
 326 65.907 and 0.377 for H₂O droplets, respectively. The values of these constants may depend on
 327 fluid thermal properties and are obtained from the experimental data of Fig. 2 (a). It was also
 328 observed in our experiments that both CAHF and H₂O droplets were pinned throughout
 329 evaporation thus exhibiting constant contact diameter (CCD) mode of evaporation. For CAHF
 330 droplets, this may be due to the hybrid nanoparticle migration towards the droplet three-phase
 331 contact line (driven by internal convection currents) that pinned the CAHF droplet resulting in
 332 CCD mode of evaporation. This also suggests that hybrid nanoparticles driven by internal
 333 convection currents deposit near the droplet three-phase contact line resulting in a pinning effect
 334 for CAHF droplet. For water droplets, the CCD mode of evaporation is possibly due to the natural
 335 convection and Marangoni forces that might have pinned the droplet on a heated surface.
 336 Moreover, the evaporation rate for CAHF droplets obtained in this study is almost similar to that
 337 reported by Xu et al. [41] for gold nanofluid droplets at similar droplet volumes and substrate
 338 temperatures. This is because hybrid nanofluid droplets do not exhibit significantly high

339 evaporation rates at low substrate temperatures (i.e., $T_s < 60$ °C) possibly due to reduced internal
340 convection effects. In another study by Yan et al. [42], the top heating of gold nanofluid droplets
341 using solar energy resulted in similar evaporation rates as that obtained for CAHF droplets in
342 current study. However, they showed that side heating of gold nanofluid droplets reduced
343 evaporation rates up to 20% than that obtained in current study for similar droplet volumes and
344 droplet surface temperatures, respectively. Furthermore, the evaporation rate of CAHF droplet at
345 substrate temperature of $T_s = 105$ °C is 13% higher than that reported by Kim [25] for CuO
346 nanofluid droplet for similar droplet volumes. However, they used nanoparticle concentration of
347 0.5% volume fraction in comparison to just 0.1% volume used in current study. Besides different
348 experimental conditions used in these studies, higher evaporation rates for hybrid nanofluid
349 droplets may be due to better heat transfer properties compared to mono nanofluids, as already
350 discussed in introduction section of this study. Furthermore, the main mechanisms involved for
351 improved evaporation rates of CAHF droplets are discussed in Section 4.1.1.

352
353 Fig. 2 (b) shows the evaporation rate of a 3 μ l CAHF droplet resting over plain copper and porous
354 residue surfaces for various residue sizes and surface temperatures. It is noticeable that the
355 evaporation rate of the following CAHF droplet on its heated residue surface for $V_{fd}/V_{sd} = 5$
356 significantly increases up to 112% compared to a heated plain copper surface for surface
357 temperatures of $T_s = 25 - 100$ °C. Further increasing the droplet volume ratio above $V_{fd}/V_{sd} = 5$
358 increases the evaporation rate of the CAHF droplet up to 141% compared to a copper surface. This
359 is for a reason that the CAHF droplet spreads on its partially wetting residue surface, exhibiting
360 large droplet-solid and droplet-air interfacial areas, which subsequently results in its high droplet
361 evaporation rate. On the other hand, the CAHF droplet resting on a non-wetted copper surface
362 exhibits a low droplet contact area, resulting in relatively lower evaporation rates compared to the
363 CAHF droplet residing over its partially wetted residue surface. The wettability effect of un-heated
364 droplet residue on subsequent droplet evaporation rate is demonstrated in our previous study [36].
365 Furthermore, the enhanced evaporation rate of the CAHF droplet over a heated plain copper
366 surface as compared to H₂O droplet (as illustrated in Fig. 2 (a)) is mainly attributed to suspended
367 hybrid nanoparticles, which may modify the internal velocity and thermal field distribution of the
368 CAHF droplet, as further discussed in Section 4.1.1.

369

370 **4.1.1. Mechanistic behavior of improved evaporation performance for CAHF droplets**

371 **4.1.1.1. Thermal conductivity and surface tension effects**

372 Fig. 3 (a) illustrates the CAHF thermal conductivity enhancement with respect to water (base fluid)
373 at different temperatures. It can be noticed that the CAHF thermal conductivity considerably
374 increases with increasing temperatures, exhibiting enhancement up to 15.5% at $T = 70$ °C. This is
375 due to enhanced thermal properties of suspended copper-alumina hybrid nanoparticles that
376 increase the overall CAHF thermal conductivity. The CAHF thermal conductivity enhancement
377 can be estimated using the following non-dimensional empirical equation:

378

$$379 \quad k_{en} = ae^{b\left(\frac{T}{T_o}\right)} \quad (5)$$

380

381 where $T_o = 20$ °C is the reference (minimum) temperature for measured thermal conductivity in
382 this study while coefficients $a = 0.0482$ and $b = 1.6218$ are obtained from measured thermal
383 conductivity data points (shown by red markers in Fig. 3 (a)).

384

385 **4.1.1.2. Droplet internal convection effects**

386 The convection effects inside the CAHF and H₂O droplets are investigated using the dynamic
387 Bond number [$Bo_d = \rho g \beta h^2 / (-d\gamma_{lv} / dT)$], where h is the droplet height, $d\gamma_{lv} / dT$ is the surface tension
388 gradient (obtained from Fig. 2 (a)), ρ and β are the density and volumetric thermal expansion
389 coefficient, respectively, obtained as $\rho = 0.5\phi\rho_{Cu} + 0.5\phi\rho_{Al_2O_3} + (1-\phi)\rho_{H_2O}$ and $\beta = -1/\rho(dp/dT)$ at
390 $[T(y = 0) + T(y = h)]/2$. The dynamic Bond number shows the relative strength of buoyancy and
391 Marangoni forces within a heated droplet. Fig. 3 illustrates the dynamic Bond number variation in
392 CAHF and H₂O droplets with normalized droplet evaporation time (t/t_o), where t_o is the net droplet
393 evaporation time. As $Bo_d < 1$ during the droplet evaporation, the Marangoni forces dominate
394 buoyancy forces in both CAHF and H₂O droplets. Moreover, increasing droplet volume increases
395 the dynamic Bond number suggesting a rise in buoyancy forces. However, as $Bo_d < 1$, the
396 buoyancy forces are still not strong enough to overcome thermal Marangoni forces within the
397 evaporating CAHF and H₂O droplets. It is also noticeable that the dynamic Bond number decreases
398 during the course of droplet evaporation indicating further weakening of the buoyancy forces.
399 Moreover, the dynamic Bond number is slightly higher for CAHF droplets than for H₂O droplets.

400 This suggests that buoyancy forces are marginally stronger in CAHF droplets possibly due to
401 higher density and volumetric expansion coefficient than that of H₂O droplets. These results also
402 indicate that the thermal Marangoni forces may affect the internal velocity and thermal field
403 distribution of CAHF and H₂O evaporating droplets. Therefore, both Marangoni and buoyancy
404 effects were considered in our droplet numerical model.

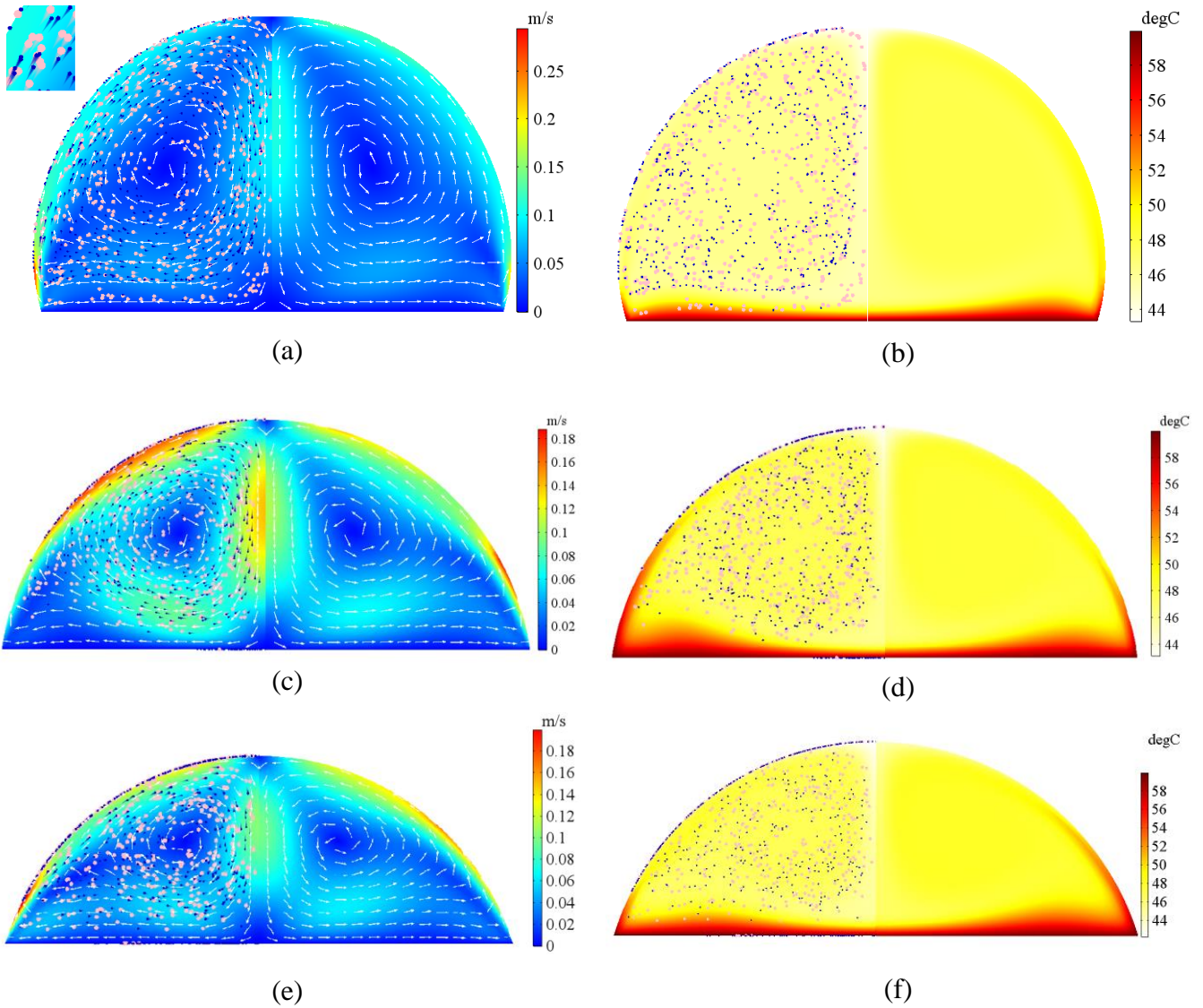
405

406 Fig. 4 shows the variation of the Marangoni number with respect to normalized droplet evaporation
407 time (t/t_o). The Marangoni number is determined as $Ma = h\Delta T(-d\gamma_{lv}/dT)/\mu\alpha$, where h is the droplet
408 height, ΔT is the temperature difference between the droplet apex and three-phase contact line
409 obtained using an infrared imaging (discussed in supplementary material), $d\gamma_{lv}/dT$ is the
410 temperature dependent surface tension gradient obtained from Fig. 3 (a), α is the thermal
411 diffusivity and μ is the dynamic viscosity (both α and μ were obtained at $[T(y = 0) + T(y = h)]/2$).
412 It is observed in Fig. 4 that the Marangoni number decreases with increasing droplet evaporation
413 time suggesting a reduction in thermal Marangoni convection for both CAHF and H₂O droplets,
414 as illustrated in Fig. 4. Furthermore, the Marangoni number considerably increases with increasing
415 droplet volume and substrate surface temperature. It is also noticeable that the Marangoni number
416 in the CAHF droplet mostly remains higher than H₂O droplet during the droplet evaporation
417 process. This suggests that enhanced thermal Marangoni convection, besides high thermal
418 conductivity, contribute towards higher evaporation rate in CAHF droplets compared to H₂O
419 droplets on a plain heated copper surface, as demonstrated in Fig. 2 (b). However, it is pertinent to
420 also compare the internal velocity and temperature fields of CAHF and H₂O droplets, as
421 demonstrated in Fig. 5 and Fig. 6.

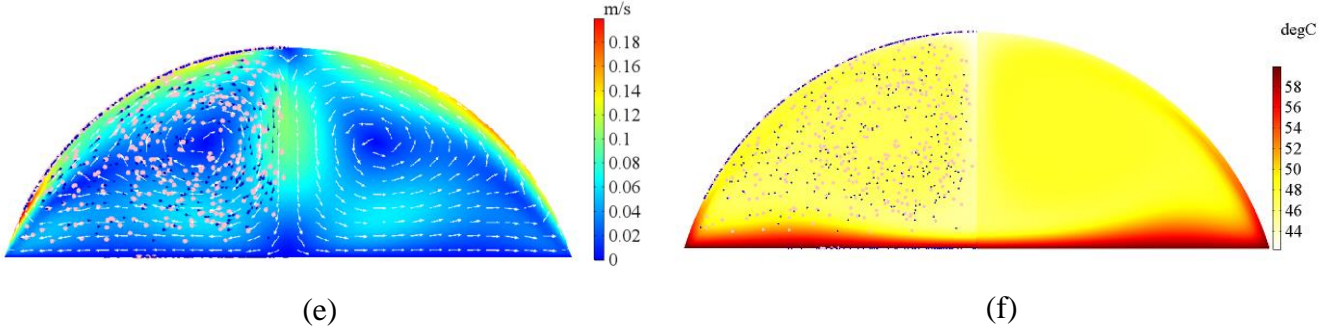
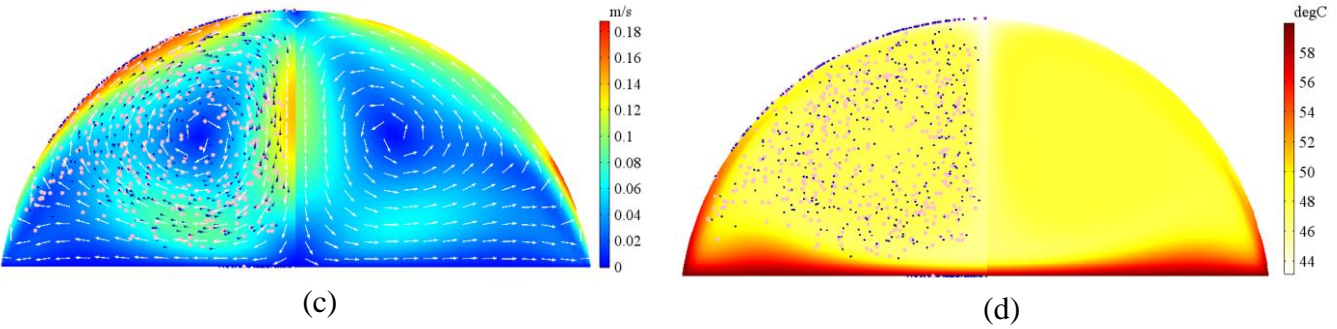
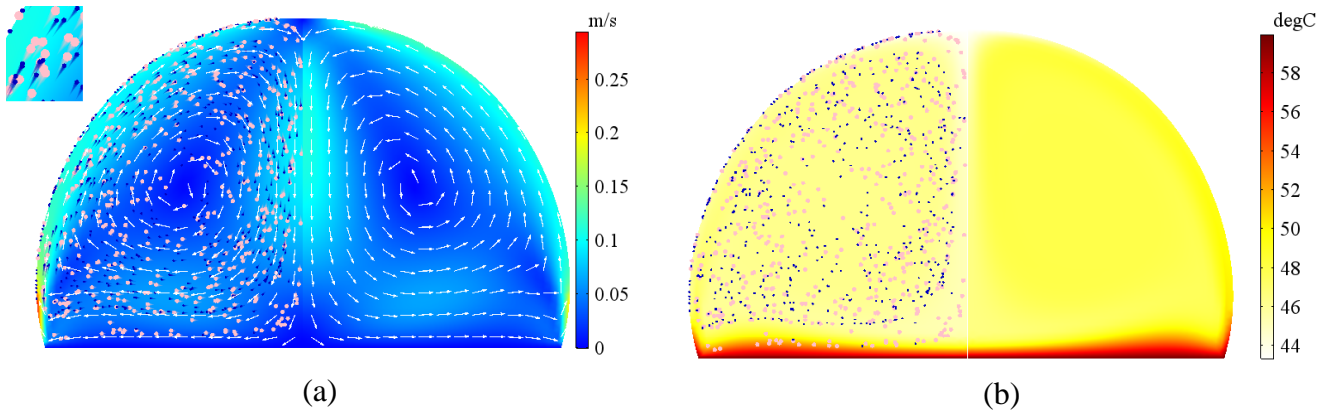
422

423 *4.1.1.3. Internal velocity and thermal field distribution of CAHF and H₂O droplets*

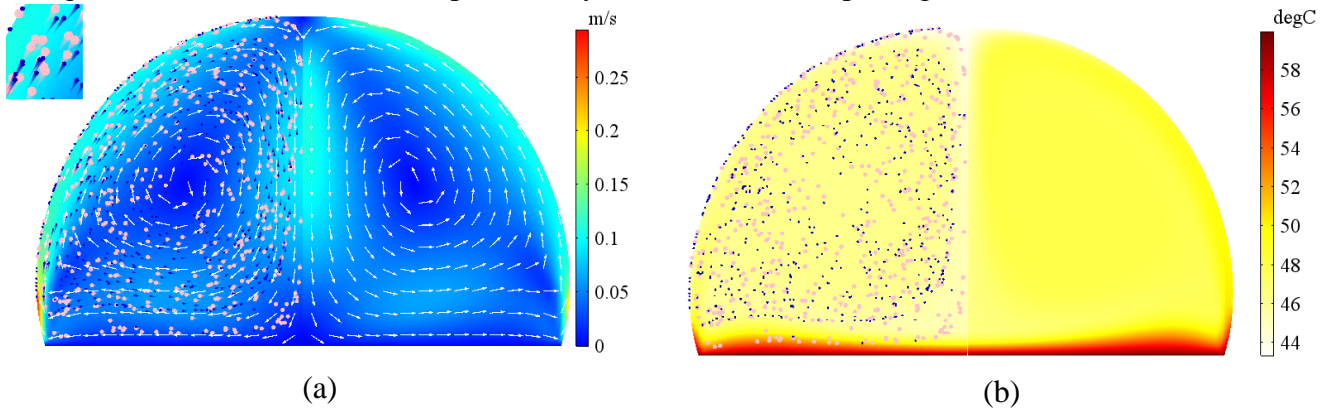
424 Fig. 5 (a) and (b) show the comparison of internal velocity and thermal field distribution between
425 the CAHF droplet (droplet left half) and H₂O droplet (droplet right half) on a plain heated copper
426 surface for $T_s = 60$ °C at the beginning of droplet evaporation process ($t = 1$ s). Although both
427 CAHF and H₂O droplets exhibit similar vortices in

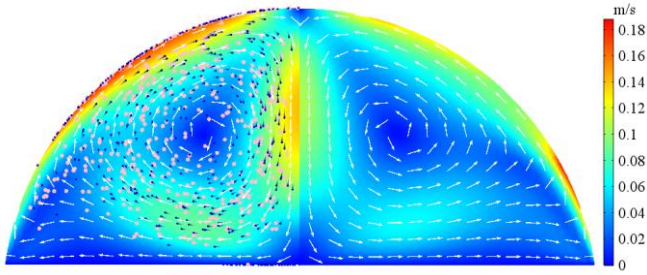


428 Fig. 5 (a), high velocity magnitude (shown by red colour) can be observed near the three-phase
 429 contact line of the CAHF droplet. This may be due to higher Marangoni convection in the CAHF
 430 droplet as compared to H₂O droplet, as demonstrated in Fig. 4. A well-mixed internal flow is
 431 developed due to high velocity magnitude inside the CAHF droplet resulting in relatively lower
 432 average internal temperature (light yellow colour in droplet left half of

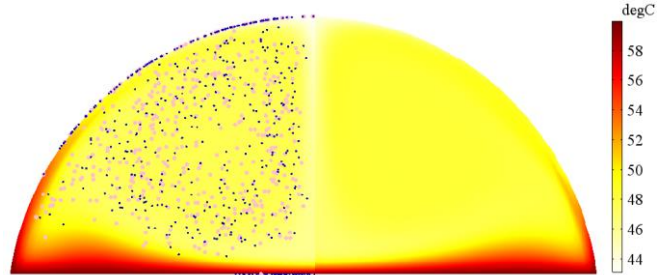


433 Fig. 5 (b)) than that of water droplet (dark yellow colour in droplet right half of

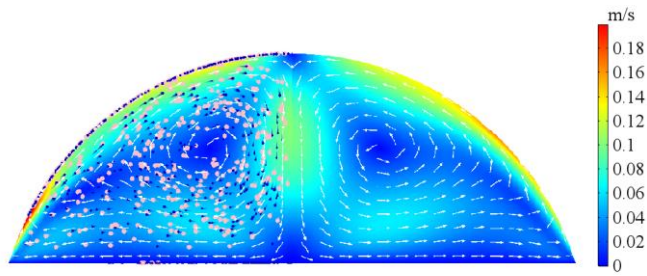




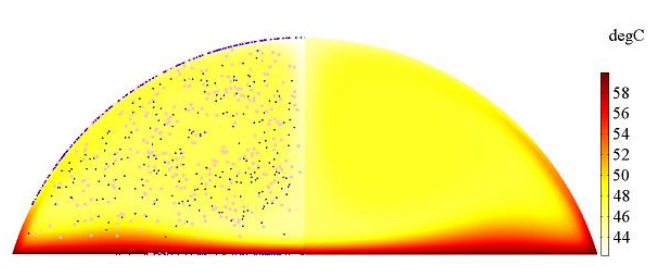
(c)



(d)

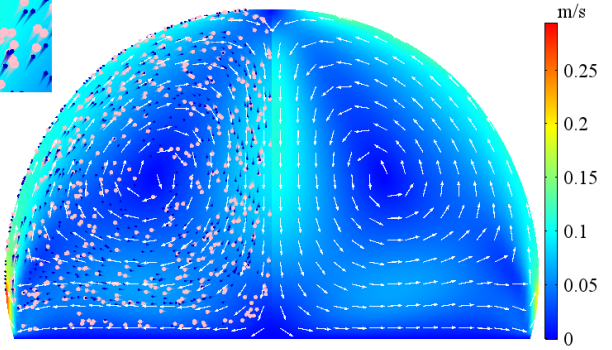


(e)

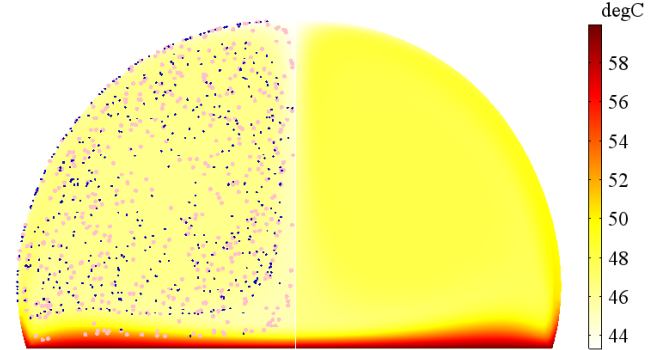


(f)

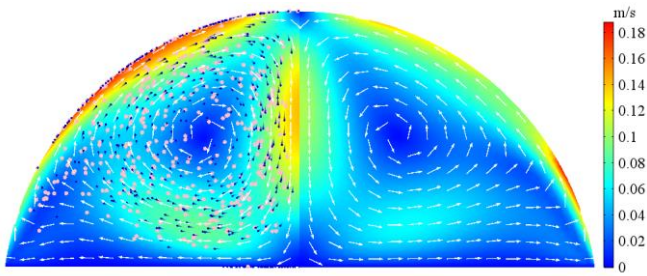
434 Fig. 5 (b)). Moreover,



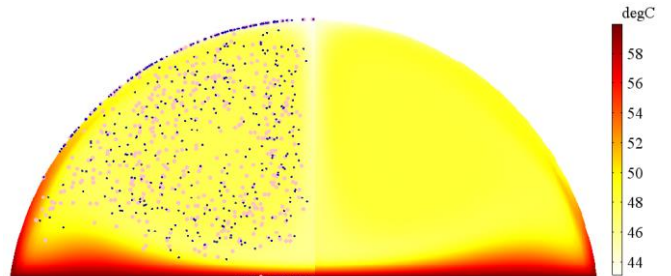
(a)



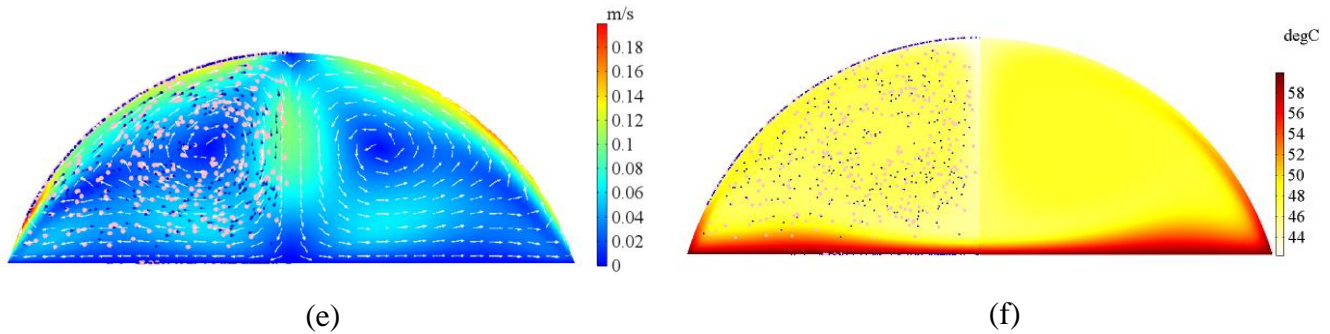
(b)



(c)



(d)



435 Fig. 5 (a) shows that the flow direction is the same (from the droplet three-phase contact line
 436 towards the droplet apex) for both CAHF and H₂O droplets. This flow direction also indicates that
 437 high Marangoni stresses (as discussed in Fig. 4) move the fluid along the thermal gradient on
 438 droplet surface. i.e., from a low surface tension region (droplet three-phase contact line) towards
 439 a high surface tension region (droplet apex). Moreover, the suspended copper (pink particles) and
 440 alumina (blue particles) nanoparticles follow the same flow direction as surrounding fluid
 441 molecules, as illustrated in droplet left half of Fig. 5 (a). Furthermore, the alumina nanoparticles
 442 exhibit higher velocity than copper nanoparticles, as shown by long blue particle tails compared
 443 to short pink particle tails in Fig. 5 (a) inset. This is because of the low density and small diameter
 444 of an alumina nanoparticle compared to a copper nanoparticle.

445
 446 Fig. 5 (c) and (d) show fluid internal velocity and thermal field for CAHF and H₂O droplets at time
 447 $t = 20$ s of the droplet evaporation process, respectively. The higher velocity magnitude can be
 448 observed for the CAHF droplet near the droplet-air interface and vertical axis of symmetry
 449 compared to H₂O droplet. Although Marangoni forces decrease with increasing droplet
 450 evaporation time (as illustrated in Fig. 4), these are still stronger in the CAHF droplet, resulting in
 451 higher velocity magnitude compared to H₂O droplet. A well-mixed internal flow due to high
 452 velocity magnitude in the CAHF droplet develops a low temperature region near the vertical axis
 453 of symmetry, as demonstrated by a light-yellow region in droplet left half of Fig. 5 (d). It is
 454 noticeable that hybrid nanoparticles move away from the high temperature zone near the droplet-
 455 solid interface (red region in Fig. 5 (d)) due to high wall shear stress and enhanced thermophoretic
 456 forces. This results in a concentration gradient with higher concentration of hybrid nanoparticles
 457 in the vortex region compared to droplet vertical axis of symmetry and interfacial (droplet-solid
 458 and droplet-air) regions, as illustrated in Fig. 5 (c). Conversely, hybrid nanoparticles are uniformly

459 distributed inside the CAHF droplet at the beginning of its evaporation ($t = 1$ s), as observed in Fig.
460 5 (a).

461
462 The fluid flow and temperature fields for CAHF and H₂O droplets at time $t = 40$ s of droplet
463 evaporation is demonstrated in Fig. 5 (e) and (f). It can be observed that the peak velocity
464 magnitude in the CAHF droplet decreases during its evaporation (low at $t = 20$ s and $t = 40$ s as
465 compared to $t = 1$ s). This may be due to increased nanoparticle concentration that increases the
466 viscosity of the CAHF droplet (as shown in equation (3)) during its evaporation. However, due to
467 high thermal Marangoni stress, the velocity magnitude near the droplet three-phase contact line is
468 still higher in the CAHF droplet compared to H₂O droplet, as demonstrated in Fig. 5 (e). Like
469 temperature distribution observed at time $t = 1$ s and $t = 20$ s, a low temperature zone in the CAHF
470 droplet near the droplet vertical axis of symmetry is noticed at time $t = 40$ s, as shown in Fig. 5 (f).
471 Moreover, in the CAHF droplet, the concentration gradient of suspended hybrid nanoparticles
472 further increases at time $t = 40$ s compared to time $t = 1$ s and $t = 20$ s. At time $t = 40$ s, a higher
473 concentration of hybrid nanoparticles near the flow vortex compared to droplet interfacial regions
474 and vertical axis of symmetry can be observed, as demonstrated in Fig. 5 (e). This high
475 concentration gradient at time $t = 40$ s creates a shear viscous flow regime resulting in reduced
476 flow velocity near the vortex region. On the other hand, high flow velocities are observed in
477 relatively low viscosity regions near droplet vertical symmetrical axis and droplet-air interface.
478 Fig. 5 corresponds to 3 μ l droplet volume at substrate temperature of $T_s = 60$ °C for which there
479 exists a negligible difference in evaporation rates between CAHF droplet and H₂O droplet, as
480 demonstrated in Fig. 2 (b). For this reason, the CAHF and H₂O droplets seems identical in Fig. 5.
481 Moreover, Fig. 5 shows droplet evaporation only up to $t = 40$ s while CAHF and H₂O droplets
482 show some difference in droplet height near the end of evaporation.

483
484 As all investigated droplet volumes (3 - 60 μ l) show similar velocity and temperature profiles over
485 a plain heated copper substrate, these results are only discussed for a 3 μ l droplet volume in Fig.
486 6. Fig. 6 (a) and (b) show fluid velocity and temperature profiles, respectively, along the droplet
487 height (h , as shown in Fig. 1 (a)) for 3 μ l volume of CAHF and H₂O droplets on a plain copper
488 surface at $T_s = 60$ °C. It is noticeable that the peak velocity magnitude in the CAHF droplet exceeds

489 the H₂O droplet peak velocity by 45% and 8% at droplet evaporation time of $t = 20$ s and $t = 40$ s,
490 respectively. The high velocity magnitude is due to stronger Marangoni forces in the CAHF droplet
491 compared to H₂O droplet, as shown in Fig. 4. This results in a well-mixed flow thus lowering the
492 mean internal temperature of the CAHF droplet compared to H₂O droplet, as shown in Fig. 6 (b).

493
494 Fig. 6 (c, d) illustrates similar velocity and temperature plots for $T_s = 80$ °C as obtained for $T_s = 60$
495 °C in Fig. 6 (a, b), where the CAHF droplet exhibits higher velocity magnitude and lower
496 temperature compared to H₂O droplet. Moreover, the velocity magnitude increases in both CAHF
497 and H₂O droplets due to the higher thermal Marangoni convection at $T_s = 80$ °C, compared to that
498 observed at $T_s = 60$ °C. In Fig. 6 (e), the CAHF droplet exhibits higher mean velocity than H₂O
499 droplet at $T_s = 100$ °C. This results in a lower mean temperature for the CAHF droplet compared
500 to the H₂O droplet at time $t = 1$ s. However, at time $t = 5$ s, this behavior is reversed where H₂O
501 droplet shows lower mean droplet temperature than the CAHF droplet, as demonstrated in Fig. 6
502 (f). This may be due to strong thermal Marangoni convection currents in both H₂O and CAHF
503 droplets at a high substrate temperature of $T_s = 100$ °C. The results of Fig. 5 and Fig. 6 suggest that
504 enhanced evaporation rate in CAHF droplets is due to higher velocity magnitude and lower mean
505 internal temperature than that of H₂O droplets. Moreover, large thermal Marangoni forces and
506 suspended hybrid nanoparticles facilitate heat transfer between the droplet-substrate and droplet-
507 air interfaces, resulting in reduced mean internal temperature and augmented evaporation rates in
508 CAHF droplets compared to H₂O droplets.

509
510 Fig. 7 (a-c) shows the comparison of fluid velocity and hybrid (copper and alumina) nanoparticle
511 velocity profiles for different time instants during evaporation of a 3 μ l CAHF droplet at $T_s = 60$
512 °C. In Fig. 7, the hybrid nanofluid droplet was treated as a non-homogenous two-phase droplet,
513 where the velocities of dispersed phase Cu and Al₂O₃ nanoparticles inside the CAHF droplet were
514 separately investigated and compared with the continuum liquid phase that surrounds the dispersed
515 hybrid nanoparticles within the CAHF droplet. As the concentration of suspended hybrid
516 nanoparticles is very low due to high shear stresses along the droplet vertical axis of symmetry (h ,
517 as shown in Fig. 1 (a)), the fluid and hybrid nanoparticle velocity profiles are compared at a slight
518 offset from the droplet vertical axis of symmetry h (i.e., at $r = 0.03 R$). It can be observed that both
519 copper and alumina nanoparticles exhibit a slip velocity, where their velocity magnitude is

520 different from surrounding fluid molecules. The hybrid nanoparticle slip may be due to
521 hydrodynamic forces (such as drag and lift forces) from surrounding fluid molecules. It is also
522 noticeable that copper nanoparticles exhibit lower average velocity with high fluctuations along
523 the droplet height than alumina nanoparticles. This may be due to the large diameter and high
524 density of copper nanoparticles compared to alumina nanoparticles. The slip in hybrid nanoparticle
525 velocity is also observed for different time instants during the CAHF droplet evaporation at $T_s =$
526 $80\text{ }^\circ\text{C}$, as demonstrated in Fig. 7 (d-f). Due to enhanced thermophoretic forces at elevated
527 temperatures, the hybrid nanoparticles exhibit higher velocity magnitude at $T_s = 80\text{ }^\circ\text{C}$ compared
528 to that at $T_s = 60\text{ }^\circ\text{C}$. Furthermore, the copper nanoparticles show a similar behavior of high
529 fluctuations with lower mean velocity than alumina nanoparticles, as observed for $T_s = 60\text{ }^\circ\text{C}$.
530 However, at $T_s = 100\text{ }^\circ\text{C}$, both copper and alumina nanoparticles exhibit large fluctuations with
531 similar mean velocity, as illustrated in Fig. 7 (g, h). This may be due to strong internal convection
532 that affects the dynamics of copper and alumina nanoparticles in a similar way at $T_s = 100\text{ }^\circ\text{C}$.
533 Although Cu and Al₂O₃ nanoparticles move at different velocities within a heated CAHF droplet
534 owing to their different densities, shape and size, their composition remains the same as initial
535 composition of 50% each. This is because only liquid part evaporates from an evaporating CAHF
536 droplet while the dispersed hybrid nanoparticles remain within the droplet and finally form a
537 residue at the end of the CAHF droplet evaporation.

538 **4.2. Boiling performance of CAHF droplets compared to H₂O droplets**

539 Fig. 8 (a) shows the evaporation rate of H₂O and CAHF droplets over a plain copper surface for
540 nucleate, transition and film boiling regimes. It is noticed that the CAHF droplet evaporation rate
541 is up to 10 times that of H₂O droplets in the nucleate boiling region. This is because the droplet
542 boiling is more vigorous and agitated due to the presence of hybrid nanoparticles in CAHF droplets
543 compared to H₂O droplets. In the nucleate boiling region, the droplet evaporation rate
544 tremendously increases at increasing substrate temperature. For considered droplet volumes, the
545 evaporation rate enhancement is up to 62 times for CAHF droplets compared to 16 times for H₂O
546 droplets on a plain copper surface with increasing surface temperature from $103\text{ }^\circ\text{C}$ to $125\text{ }^\circ\text{C}$. This
547 suggests a tremendous amount of heat can be removed using CAHF droplets due to their
548 significantly high evaporation rates, making them more suitable for effective cooling of high flux
549 devices compared to water droplets. In droplet boiling experiments, the highest droplet evaporation

550 rate was obtained at the critical point (C_p), as illustrated in Fig. 8 (a). However, two critical points
551 ($C_{p,1}$ and $C_{p,2}$) are observed depending on CAHF and H₂O droplet volumes. The 3 μ l and 15 μ l
552 volume droplets enter transition boiling regime at relatively lower surface temperatures ($C_{p,1}$) than
553 30 μ l and 60 μ l volume droplets ($C_{p,2}$). This is because small droplets have reduced effective
554 contact area with the heated surface than large droplets due to the presence of bubbles at the
555 droplet-solid interface. Increasing substrate temperature beyond the critical point further decreases
556 the droplet contact area until a Leidenfrost point (L_p) is reached, where droplet rolls over the vapour
557 cushion on a copper surface (Leidenfrost effect) resulting in low evaporation rates, as illustrated
558 in Fig. 8 (a). The CAHF and H₂O droplets exhibit almost the same evaporation rates in the film-
559 boiling region as they both experience the Leidenfrost effect.

560
561 Fig. 8 (b) shows evaporation rate of a 3 μ l CAHF droplet over plain copper and porous residue
562 surfaces for nucleate boiling region. As droplets move over a heated surface in transition boiling
563 and film boiling regions, the residue effect on the following droplet evaporation rate is only studied
564 in the nucleate boiling regime. It is noticeable that the CAHF droplet evaporation rate is enhanced
565 up to 9 times on a porous residue surface compared to a plain copper surface. This is mainly due
566 to higher droplet spreading over a partially wetted residue surface compared to a non-wetted
567 copper surface. However, the effect of droplet residue size ($V_{fd}/V_{sd} = 5, 10$ and 20) on the
568 subsequent droplet evaporation rate is not very clear due to a non-uniform residue surface obtained
569 in the nucleate boiling region.

570

571 **4.2.1. Mechanistic behaviour of improved boiling performance for CAHF droplets**

572 **4.2.1.1. Latent heat flux**

573 Fig. 9 demonstrates the latent heat flux for various volumes of H₂O droplets over a plain copper
574 surface and CAHF droplets over plain copper and porous residue surfaces ($V_{fd}/V_{sd} = 20$) in the
575 nucleate boiling region. The droplet latent heat flux is only studied in the nucleate boiling region
576 as higher evaporation rates are achieved in this region compared to transition or film boiling
577 regimes. The droplet latent heat flux is obtained as $Q = \rho E h_{fg} / A_c$, where h_{fg} is the latent heat of
578 vaporization ($h_{fg,CAHF} = 2330.1 \pm 48.3$ kJ/kg and $h_{fg,H2O} = 2259 \pm 25.8$ kJ/kg), A_c is the droplet-
579 substrate interfacial area, E is the evaporation rate of the boiling droplet and ρ is the water density
580 (since only water from CAHF droplet evaporates leaving behind a residue of hybrid nanoparticles).

581 It can be observed in Fig. 9 that the latent heat flux increases with increasing substrate temperature
582 for both CAHF and H₂O droplets, exhibiting the maximum heat flux at $T_s = 125$ °C. Moreover,
583 increasing droplet volume leads to decreasing latent heat flux for both CAHF and H₂O droplets
584 due to the increase in droplet-solid contact area. Despite such similarities between CAHF and H₂O
585 droplets, CAHF droplets exhibit substantially higher latent heat flux than H₂O droplets for similar
586 droplet volumes in the nucleate boiling region, as demonstrated in Fig. 9. It is noticeable that the
587 latent heat flux up to 10 times can be achieved using the CAHF droplet compared to H₂O droplet
588 on a plain heated copper surface. This is due to high latent heat of vaporization along with
589 enhanced evaporation rate resulting in augmented heat flux in CAHF droplets compared to H₂O
590 droplets. This shows enhanced heat removal capability of CAHF droplets at even low particle
591 concentration of 0.1% volume fraction compared to H₂O droplets. These results also suggest that
592 the CAHF can be a better candidate than existing fluids (for instance water) for droplet-based
593 (spray or hotspot) cooling in high heat flux applications. Furthermore, despite higher evaporation
594 rate of the CAHF droplet on its porous residue surface than on a plain copper surface (as illustrated
595 in Fig. 8 (b)), the latent heat flux of a 3 μ l CAHF droplet over a residue surface is less than that on
596 a plain copper surface, as shown in Fig. 9. This is because the subsequent CAHF droplet spreads
597 more on its partially wetting residue surface than on a non-wetted copper surface, as shown in Fig.
598 9 insets. This increases the droplet-solid contact area of the CAHF droplet over the residue surface
599 resulting in reduced latent heat flux.

600

601 **4.2.1.2. Boiling dynamics**

602 Fig. 10 demonstrates the comparison between boiling dynamics of the CAHF droplet and H₂O
603 droplet over a heated copper surface in the nucleate boiling regime. For a water droplet at $T_s = 105$
604 °C, it can be observed that bubble nucleation starts at $t = 0.16$ s. At $t = 1.44$ s, multiple bubbles can
605 be observed suggesting several nucleation sites at the droplet-solid interface inside the water
606 droplet. At $t = 2.4$ s, the bubbles merge into a big bubble that eventually bursts and escapes the
607 water droplet surface. However, the water droplet still maintains its spherical shape despite
608 multiple events of bubble formation and collapse during the droplet boiling process. Conversely,
609 the CAHF droplet experiences shape variations during droplet boiling at $T_s = 105$ °C. This is due
610 to the suspension of thermally conductive copper-alumina hybrid nanoparticles within the CAHF
611 droplet transferring their high thermal energy to surrounding water molecules that disrupt the

612 CAHF droplet shape. Consequently, the CAHF droplet ejects a few small droplets as observed at
613 $t = 2.52\text{s}$ and $t = 4.36\text{s}$, which is not the case with the H_2O droplet at $T_s = 105\text{ }^\circ\text{C}$. At $T_s = 115\text{ }^\circ\text{C}$,
614 the bubbles are observed inside the water droplet at $t = 0.63\text{s}$ that eventually grow and occupy the
615 water droplet surface, as observed at $t = 10.32\text{s}$. As bubbles reach the water droplet surface, the
616 nucleation sites are available at droplet-solid interface for new bubbles to form and grow, as
617 demonstrated at $t = 10.32\text{s}$. The bubbles at water droplet surface eventually burst and more bubbles
618 from nucleation sites grow and occupy the water droplet surface, as noticed at $t = 14.6\text{s}$. This
619 process continues until the water droplet completely evaporates. The high density of bubbles inside
620 the water droplet offers thermal resistance that slows down the droplet boiling process. Unlike
621 water droplet at $T_s = 115\text{ }^\circ\text{C}$, the CAHF droplet exhibits early shape variations and eject multiple
622 small droplets due to the agitation induced by suspended copper-alumina hybrid nanoparticles, as
623 observed at $t = 0.33\text{s}$ and $t = 1.18\text{s}$. The increasing hybrid nanoparticle concentration with
624 progressive evaporation of the CAHF droplet induces further agitation that erupts numerous tiny
625 droplets resulting in rapid droplet evaporation, as demonstrated at $t = 2\text{s}$ and $t = 2.06\text{s}$. At $T_s = 125$
626 $^\circ\text{C}$, the highly agitated H_2O and CAHF droplets release multiple small droplets resulting in high
627 droplet evaporation rate. However, early initiation of multiple droplet ejection process due to
628 suspended hybrid nanoparticles evaporates the CAHF droplet long before the water droplet.
629 Moreover, part of the CAHF droplet instantaneously lifts-off the heated copper surface releasing
630 energy from thermally conductive hybrid nanoparticles, as observed at $t = 0.06\text{s}$. Upon subsequent
631 re-contact of droplet lift-off part with the heated copper surface, several tiny droplets are released,
632 as demonstrated at $t = 0.1\text{s}$. The instantaneous lift-off and re-contact process continue until the end
633 of the CAHF droplet boiling. Conversely, at $T_s = 125\text{ }^\circ\text{C}$, the water droplet does not exhibit the
634 lift-off mechanism, suggesting relatively low agitation that delays its evaporation time compared
635 to the CAHF droplet.

636

637 **5. Conclusions**

638 Despite high cooling efficiency of droplet evaporation based cooling technologies, for instance
639 spray cooling, the existing fluids (for instance water) may not be used in such technologies for
640 thermal management of modern high heat flux devices due to their limited cooling capacity. To
641 tackle this problem, as a novelty of this research, we experimentally studied the evaporation and
642 boiling of CAHF droplets on plain copper and porous residue surfaces, formed by the evaporation

643 of the first CAHF droplet on a plain copper surface. We demonstrated that the evaporation rate
644 was substantially improved for CAHF droplets resting on their partially wetting residue surfaces
645 compared to a non-wetted copper surface in sub-boiling and nucleate boiling regimes. As a
646 benchmark, we compared the CAHF droplet evaporation and boiling results with water droplets.
647 We also reported that high thermal Marangoni convection, besides high thermal conductivity,
648 contributes towards higher evaporation rates in CAHF droplets compared to water droplets.
649 Furthermore, we numerically investigated and compared the velocity and temperature fields of
650 CAHF and H₂O droplets. We investigated droplet evaporation rate for three different boiling
651 regimes (nucleate, transition and film boiling regimes), while mainly focusing on the nucleate
652 boiling regime for exhibiting substantially higher droplet evaporation rates than other boiling
653 regimes. The following are the key outcomes of this research:

- 654 • The evaporation rate of CAHF droplets is enhanced up to 24% that of water droplets over
655 a plain copper substrate for $T_s = 25-100$ °C.
- 656 • In the nucleate boiling region, the CAHF droplet evaporation rate is enhanced up to 13
657 times that of water droplets.
- 658 • The latent heat flux up to 10 times can be achieved using the CAHF droplets compared to
659 H₂O droplets on a plain copper surface in the nucleate boiling regime.
- 660 • The evaporation rate of the following CAHF droplet on a residue surface rises up to 141%
661 and 800% that on a plain copper surface in sub-boiling and nucleate boiling regimes,
662 respectively.
- 663 • The high thermal Marangoni convection in CAHF droplets results in higher internal
664 velocity and lower internal mean temperature than H₂O droplets.

665

666 **Acknowledgements**

667 The funding for this research is provided by the Hong Kong PhD Fellowship Scheme (HKPFS),
668 the Hong Kong Research Grant Council via Collaborative Research Fund (CRF) account C6022-
669 16G, General Research Fund (GRF) accounts 16206918 & 17205419 and Early Career Scheme
670 (ECS) account 21200819.

671

672 **References**

673 [1] C.Y. Tso, C.Y.H. Chao, Study of enthalpy of evaporation, saturated vapor pressure and

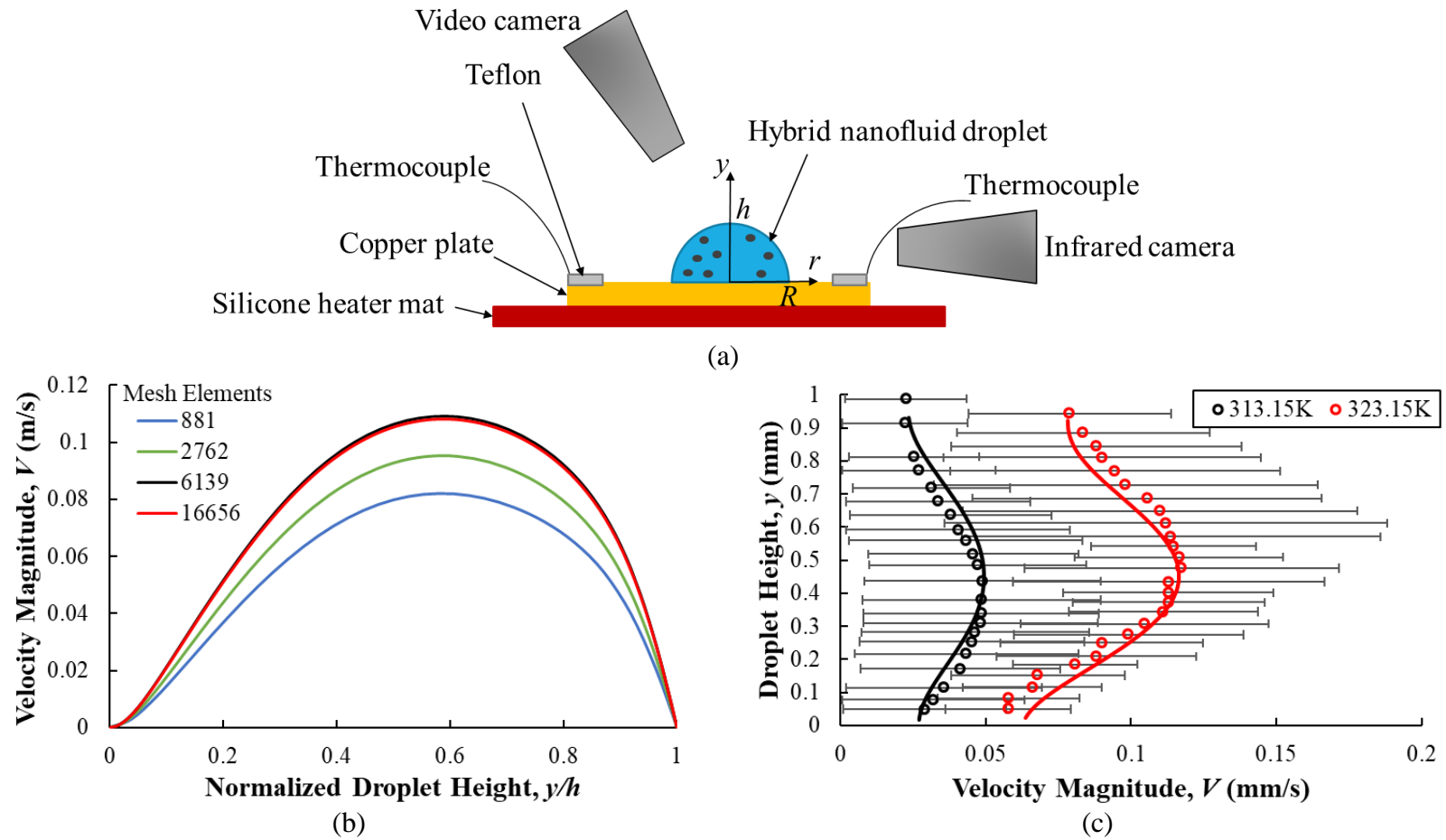
- 674 evaporation rate of aqueous nanofluids, *Int. J. Heat Mass Transf.* 84 (2015) 931–941.
675 <https://doi.org/10.1016/j.ijheatmasstransfer.2015.01.090>.
- 676 [2] S. Fu, C. Tso, Y. Fong, C.Y.H. Chao, Evaporation of Al₂O₃-water nanofluids in an
677 externally micro-grooved evaporator, *Sci. Technol. Built Environ.* 23 (2017) 345–354.
678 <https://doi.org/10.1080/23744731.2016.1250562>.
- 679 [3] C.Y. Tso, S.C. Fu, C.Y.H. Chao, A semi-analytical model for the thermal conductivity of
680 nanofluids and determination of the nanolayer thickness, *Int. J. Heat Mass Transf.* 70
681 (2014) 202–214. <https://doi.org/https://doi.org/10.1016/j.ijheatmasstransfer.2013.10.077>.
- 682 [4] S. Kakac, A. Pramuanjaroenkij, Analysis Of Convective Heat Transfer Enhancement By
683 Nanofluids: Single-Phase And Two-Phase Treatments, *J. Eng. Phys. Thermophys.* 89
684 (2016) 758–793. <https://doi.org/10.1007/s10891-016-1437-1>.
- 685 [5] D. Yoo, Thermal Conductivity of Al₂O₃/Water Nanofluids, *J. Korean Phys. Soc.* 51
686 (2007) 84–87.
- 687 [6] S. Akilu, K. V. Sharma, A.T. Baheta, R. Mamat, A review of thermophysical properties of
688 water based composite nanofluids, *Renew. Sustain. Energy Rev.* 66 (2016) 654–678.
689 <https://doi.org/10.1016/j.rser.2016.08.036>.
- 690 [7] F.R. Siddiqui, C.Y. Tso, K.C. Chan, S.C. Fu, C.Y.H. Chao, Dataset on critical parameters
691 of dispersion stability of Cu/Al₂O₃ nanofluid and hybrid nanofluid for various ultra-
692 sonication times, *Data Br.* 22 (2019) 863–865.
- 693 [8] L. Yang, J. Xu, K. Du, X. Zhang, Recent developments on viscosity and thermal
694 conductivity of nanofluids, *Powder Technol.* 317 (2017) 348–369.
695 <https://doi.org/10.1016/j.powtec.2017.04.061>.
- 696 [9] F.R. Siddiqui, C.Y. Tso, K.C. Chan, S.C. Fu, C.Y.H. Chao, On trade-off for dispersion
697 stability and thermal transport of Cu-Al₂O₃ hybrid nanofluid for various mixing ratios,
698 *Int. J. Heat Mass Transf.* 132 (2019) 1200–1216.
699 <https://doi.org/https://doi.org/10.1016/j.ijheatmasstransfer.2018.12.094>.
- 700 [10] M.J. Nine, H. Chung, M.R. Tanshen, N.A.B.A. Osman, H. Jeong, Is metal nanofluid
701 reliable as heat carrier?, *J. Hazard. Mater.* 273 (2014) 183–191.

- 702 <https://doi.org/10.1016/j.jhazmat.2014.03.055>.
- 703 [11] J.A.R. Babu, K.K. Kumar, S.S. Rao, State-of-art review on hybrid nanofluids, *Renew.*
704 *Sustain. Energy Rev.* 77 (2017) 551–565. <https://doi.org/10.1016/j.rser.2017.04.040>.
- 705 [12] J. Sarkar, P. Ghosh, A. Adil, A review on hybrid nanofluids: Recent research,
706 development and applications, *Renew. Sustain. Energy Rev.* 43 (2015) 164–177.
707 <https://doi.org/https://doi.org/10.1016/j.rser.2014.11.023>.
- 708 [13] N.A. Che Sidik, M. Mahmud Jamil, W.M.A. Aziz Japar, I. Muhammad Adamu, A review
709 on preparation methods, stability and applications of hybrid nanofluids, *Renew. Sustain.*
710 *Energy Rev.* (2017). <https://doi.org/10.1016/j.rser.2017.05.221>.
- 711 [14] M.U. Sajid, H.M. Ali, Thermal conductivity of hybrid nanofluids : A critical review, *Int. J.*
712 *Heat Mass Transf.* 126 (2018) 211–234.
713 <https://doi.org/10.1016/j.ijheatmasstransfer.2018.05.021>.
- 714 [15] M. Batmunkh, M.R. Tanshen, M.J. Nine, M. Myekhlai, H. Choi, H. Chung, Thermal
715 Conductivity of TiO₂ Nanoparticles Based Aqueous Nanofluids with an Addition of a
716 Modified Silver Particle, *Ind. Eng. Chem. Res.* 53 (2014) 8445–8451.
717 <https://doi.org/10.1021/ie403712f>.
- 718 [16] M.J. Nine, M. Batmunkh, J.H. Kim, H.S. Chung, H.M. Jeong, Investigation of Al₂O₃-
719 MWCNTs Hybrid Dispersion in Water and Their Thermal Characterization, *J. Nanosci.*
720 *Nanotechnol.* 12 (2012) 4553–4559. <https://doi.org/10.1166/jnn.2012.6193>.
- 721 [17] S. Suresh, K.P. Venkataraj, P. Selvakumar, M. Chandrasekar, Synthesis of Al₂O₃-
722 Cu/water hybrid nanofluids using two step method and its thermo physical properties,
723 *Colloids Surfaces A Physicochem. Eng. Asp.* 388 (2011) 41–48.
724 <https://doi.org/https://doi.org/10.1016/j.colsurfa.2011.08.005>.
- 725 [18] T.A.H. Nguyen, A. V Nguyen, Increased Evaporation Kinetics of Sessile Droplets by
726 Using Nanoparticles, *Langmuir.* 28 (2012) 16725–16728.
727 <https://doi.org/10.1021/la303293w>.
- 728 [19] F.C. Wang, H.A. Wu, Pinning and depinning mechanism of the contact line during
729 evaporation of nano-droplets sessile on textured surfaces, *Soft Matter.* 9 (2013) 5703–

- 730 5709. <https://doi.org/10.1039/C3SM50530H>.
- 731 [20] R.H. Chen, T.X. Phuoc, D. Martello, Effects of nanoparticles on nanofluid droplet
732 evaporation, *Int. J. Heat Mass Transf.* 53 (2010) 3677–3682.
733 <https://doi.org/https://doi.org/10.1016/j.ijheatmasstransfer.2010.04.006>.
- 734 [21] F.R. Siddiqui, C.Y. Tso, S.C. Fu, C.Y.H. Chao, H.H. Qiu, Experimental Investigation On
735 Silver-Graphene Hybrid Nanofluid Droplet Evaporation And Wetting Characteristics Of
736 Its Nanostructured Droplet Residue, in: *Proc. ASME-JSME-KSME 8th Jt. Fluids Eng.*
737 *Conf.*, San Francisco, California, USA. July 28–August 1, 2019. Paper No:
738 AJKFluids2019-5049, V004T06A010, 2019.
739 <https://doi.org/https://doi.org/10.1115/AJKFluids2019-5049>.
- 740 [22] F.R. Siddiqui, C.Y. Tso, S.C. Fu, H.H. Qiu, C.Y.H. Chao, Evaporation and wetting
741 behavior of silver-graphene hybrid nanofluid droplet on its porous residue surface for
742 various mixing ratios, *Int. J. Heat Mass Transf.* 153 (2020) 119618.
743 <https://doi.org/https://doi.org/10.1016/j.ijheatmasstransfer.2020.119618>.
- 744 [23] H. Hu, R.G. Larson, Evaporation of a Sessile Droplet on a Substrate, *J. Phys. Chem. B.*
745 106 (2002) 1334–1344. <https://doi.org/10.1021/jp0118322>.
- 746 [24] K. Sefiane, R. Bennacer, Nanofluids droplets evaporation kinetics and wetting dynamics
747 on rough heated substrates, *Adv. Colloid Interface Sci.* 147–148 (2009) 263–271.
748 <https://doi.org/https://doi.org/10.1016/j.cis.2008.09.011>.
- 749 [25] Y.C. Kim, Evaporation of nanofluid droplet on heated surface, *Adv. Mech. Eng.* 7 (2015)
750 1–8. <https://doi.org/10.1177/1687814015578358>.
- 751 [26] A. Al-Sharafi, A.Z. Sahin, B.S. Yilbas, S.Z. Shuja, Marangoni convection flow and heat
752 transfer characteristics of water–CNT nanofluid droplets, *Numer. Heat Transf. Part A*
753 *Appl.* 69 (2016) 763–780. <https://doi.org/10.1080/10407782.2015.1090809>.
- 754 [27] A. Al-Sharafi, H. Ali, B.S. Yilbas, A.Z. Sahin, M. Khaled, N. Al-Aqeeli, F. Al-Sulaiman,
755 Influence of thermalcapillary and buoyant forces on flow characteristics in a droplet on
756 hydrophobic surface, *Int. J. Therm. Sci.* 102 (2016) 239–253.
757 <https://doi.org/https://doi.org/10.1016/j.ijthermalsci.2015.11.013>.

- 758 [28] T. Okawa, K. Nagano, T. Hirano, Boiling heat transfer during single nanofluid drop
759 impacts onto a hot wall, *Exp. Therm. Fluid Sci.* 36 (2012) 78–85.
760 <https://doi.org/https://doi.org/10.1016/j.expthermflusci.2011.08.007>.
- 761 [29] G. Duursma, K. Sefiane, A. Kennedy, Experimental Studies of Nanofluid Droplets in
762 Spray Cooling, *Heat Transf. Eng.* 30 (2009) 1108–1120.
763 <https://doi.org/10.1080/01457630902922467>.
- 764 [30] G. Paul, P.K. Das, I. Manna, Nanoparticle deposition from nanofluid droplets during
765 Leidenfrost phenomenon and consequent rise in transition temperature, *Int. J. Heat Mass*
766 *Transf.* 148 (2020) 119110.
767 <https://doi.org/https://doi.org/10.1016/j.ijheatmasstransfer.2019.119110>.
- 768 [31] F.R. Siddiqui, C.Y. Tso, S.C. Fu, H.H. Qiu, C.Y.H. Chao, Droplet evaporation and boiling
769 for different mixing ratios of the silver-graphene hybrid nanofluid over heated surfaces,
770 *Int. J. Heat Mass Transf.* 180 (2021) 121786.
771 <https://doi.org/https://doi.org/10.1016/j.ijheatmasstransfer.2021.121786>.
- 772 [32] P.J. Yunker, T. Still, M.A. Lohr, A.G. Yodh, Suppression of the coffee-ring effect by
773 shape-dependent capillary interactions, *Nature.* 476 (2011) 308–311.
774 <https://doi.org/10.1038/nature10344>.
- 775 [33] T.P. Bigioni, X.M. Lin, T.T. Nguyen, E.I. Corwin, T.A. Witten, H.M. Jaeger, Kinetically
776 driven self assembly of highly ordered nanoparticle monolayers, *Nat. Mater.* 5 (2006)
777 265–270. <https://doi.org/10.1038/nmat1611>.
- 778 [34] H.H. Lee, S.C. Fu, C.Y. Tso, C.Y.H. Chao, Study of residue patterns of aqueous nanofluid
779 droplets with different particle sizes and concentrations on different substrates, *Int. J. Heat*
780 *Mass Transf.* 105 (2017) 230–236.
781 <https://doi.org/https://doi.org/10.1016/j.ijheatmasstransfer.2016.09.093>.
- 782 [35] M. Amjad, Y. Yang, G. Raza, H. Gao, J. Zhang, L. Zhou, X. Du, D. Wen, Deposition
783 pattern and tracer particle motion of evaporating multi-component sessile droplets, *J.*
784 *Colloid Interface Sci.* 506 (2017) 83–92.
785 <https://doi.org/https://doi.org/10.1016/j.jcis.2017.07.025>.

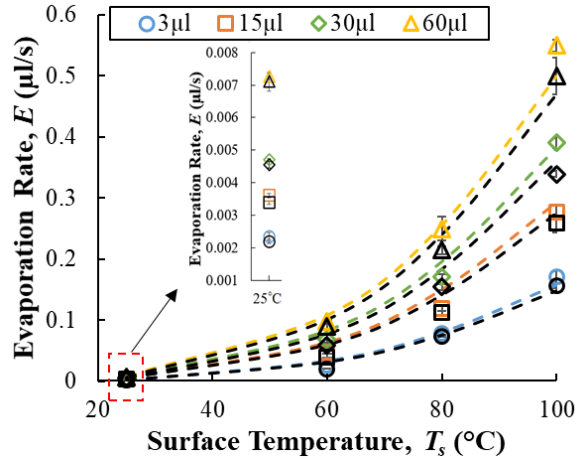
- 786 [36] F.R. Siddiqui, C.Y. Tso, S.C. Fu, H. Qiu, C.Y.H. Chao, Droplet Evaporation of Cu–
787 Al₂O₃ Hybrid Nanofluid Over Its Residue and Copper Surfaces: Toward Developing a
788 New Analytical Model, *J. Heat Transfer*. 143 (2021) 1–11.
789 <https://doi.org/10.1115/1.4048970>.
- 790 [37] C.J. Ho, J.B. Huang, P.S. Tsai, Y.M. Yang, Preparation and properties of hybrid water-
791 based suspension of Al₂O₃ nanoparticles and MEPCM particles as functional forced
792 convection fluid, *Int. Commun. Heat Mass Transf.* 37 (2010) 490–494.
793 <https://doi.org/https://doi.org/10.1016/j.icheatmasstransfer.2009.12.007>.
- 794 [38] M. Bahiraei, Particle migration in nanofluids: A critical review, *Int. J. Therm. Sci.* 109
795 (2016) 90–113. <https://doi.org/10.1016/j.ijthermalsci.2016.05.033>.
- 796 [39] M. Bahiraei, S.M. Hosseinalipour, Particle migration in nanofluids considering
797 thermophoresis and its effect on convective heat transfer, *Thermochim. Acta.* 574 (2013)
798 47–54. <https://doi.org/10.1016/j.tca.2013.09.010>.
- 799 [40] L. Karlsson, A. Ljung, T.S. Lundstrom, Comparing Internal Flow in Freezing and
800 Evaporating Water Droplets Using PIV, *Water*. 12 (2020) 1489.
801 <https://doi.org/10.3390/w12051489>.
- 802 [41] J. Xu, X. Yan, G. Liu, J. Xie, The critical nanofluid concentration as the crossover
803 between changed and unchanged solar-driven droplet evaporation rates, *Nano Energy.* 57
804 (2019) 791–803. <https://doi.org/10.1016/j.nanoen.2019.01.013>.
- 805 [42] X. Yan, J. Xu, Z. Meng, J. Xie, G. Liu, Multiscale Characteristic in
806 Symmetric/Asymmetric Solar-Driven Nanofluid Droplet Evaporation, *Langmuir.* 36
807 (2020) 1680–1690. <https://doi.org/10.1021/acs.langmuir.9b03122>.
- 808



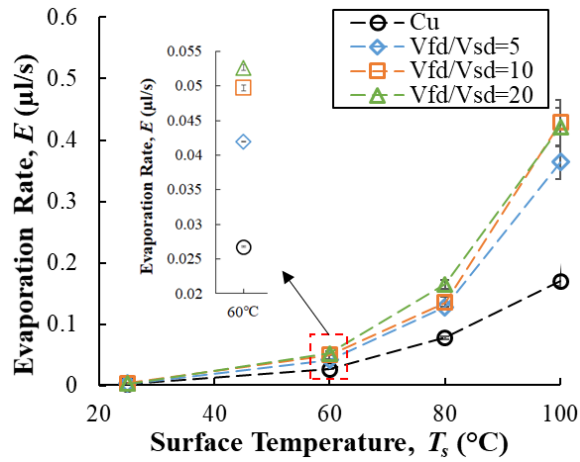
810

811 Fig. 1 (a) A schematic of the experimental setup, (b) mesh independence test for the CAHF droplet simulation and (c) numerical
 812 model validation using experimental velocity data at $r = 0$ [40]

813



(a)



(b)

814

815

816

817

818

819

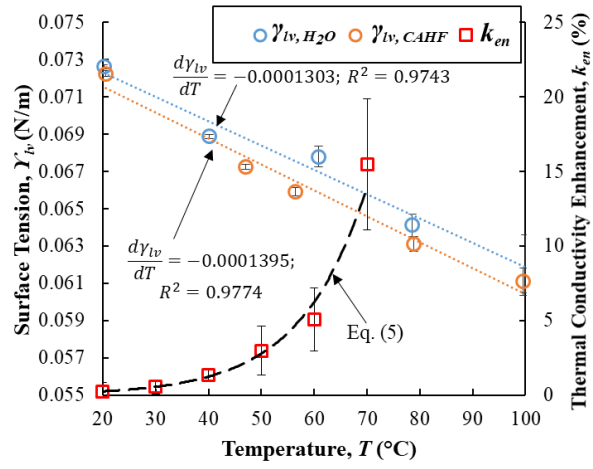
820

821

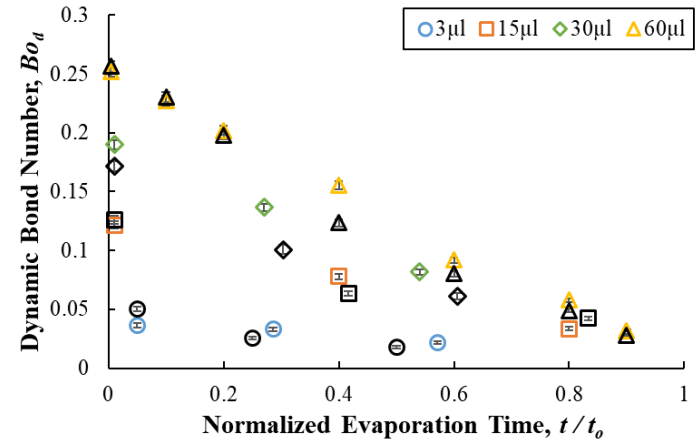
822

823

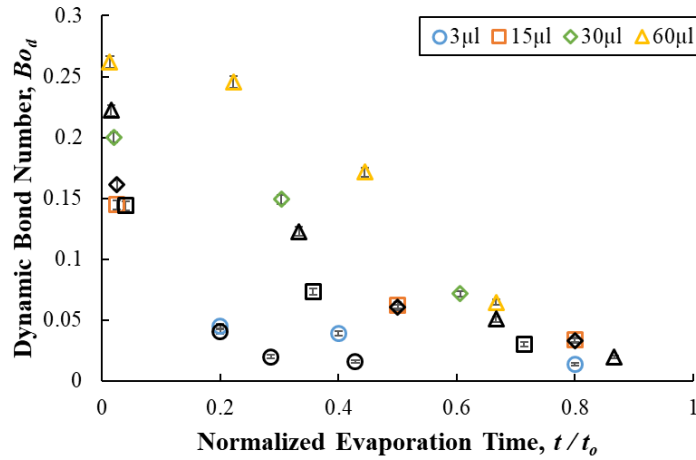
Fig. 2 (a) Evaporation rate of H₂O droplets (black markers) and CAHF droplets (colored markers) on a copper surface for different droplet volumes. Dashed lines (black for H₂O droplets and colored for CAHF droplets) are empirical results from equation (4), (b) evaporation rate of a 3 μl volume of the CAHF droplet over copper (black marker) and residue surfaces (colored markers) for various substrate temperatures.



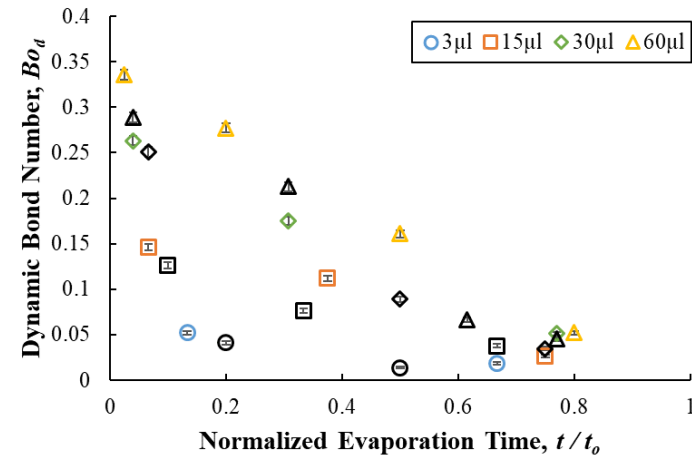
(a)



(b)



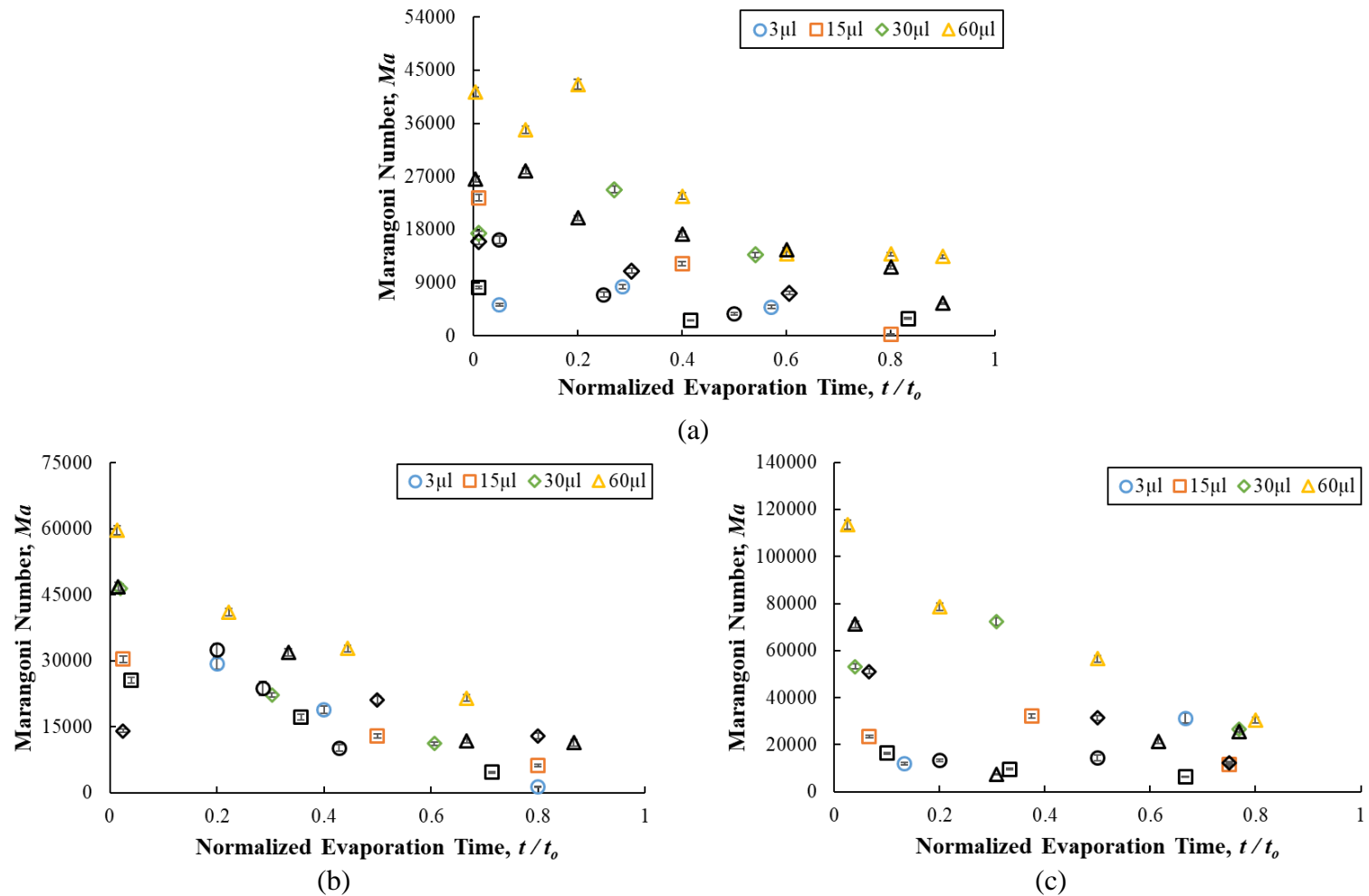
(c)



(d)

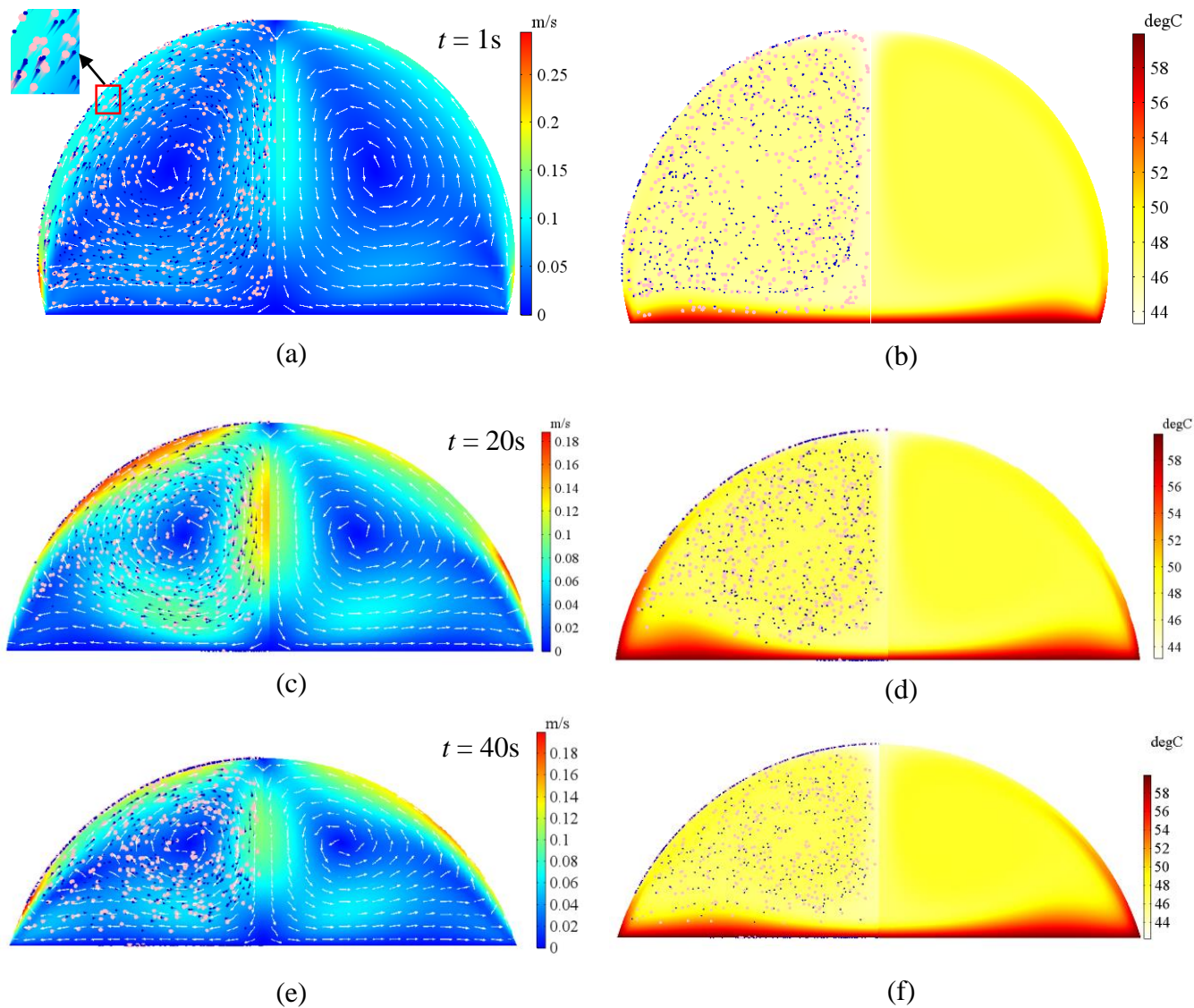
824 Fig. 3 (a) CAHF and H₂O surface tension and thermal conductivity plots, (b-d) variation of the dynamic Bond number with
 825 evaporation time of H₂O droplets (black markers) and CAHF droplets (colored markers) at a copper plate surface temperature of (b)
 826 60 °C, (c) 80 °C and (d) 100 °C.

827



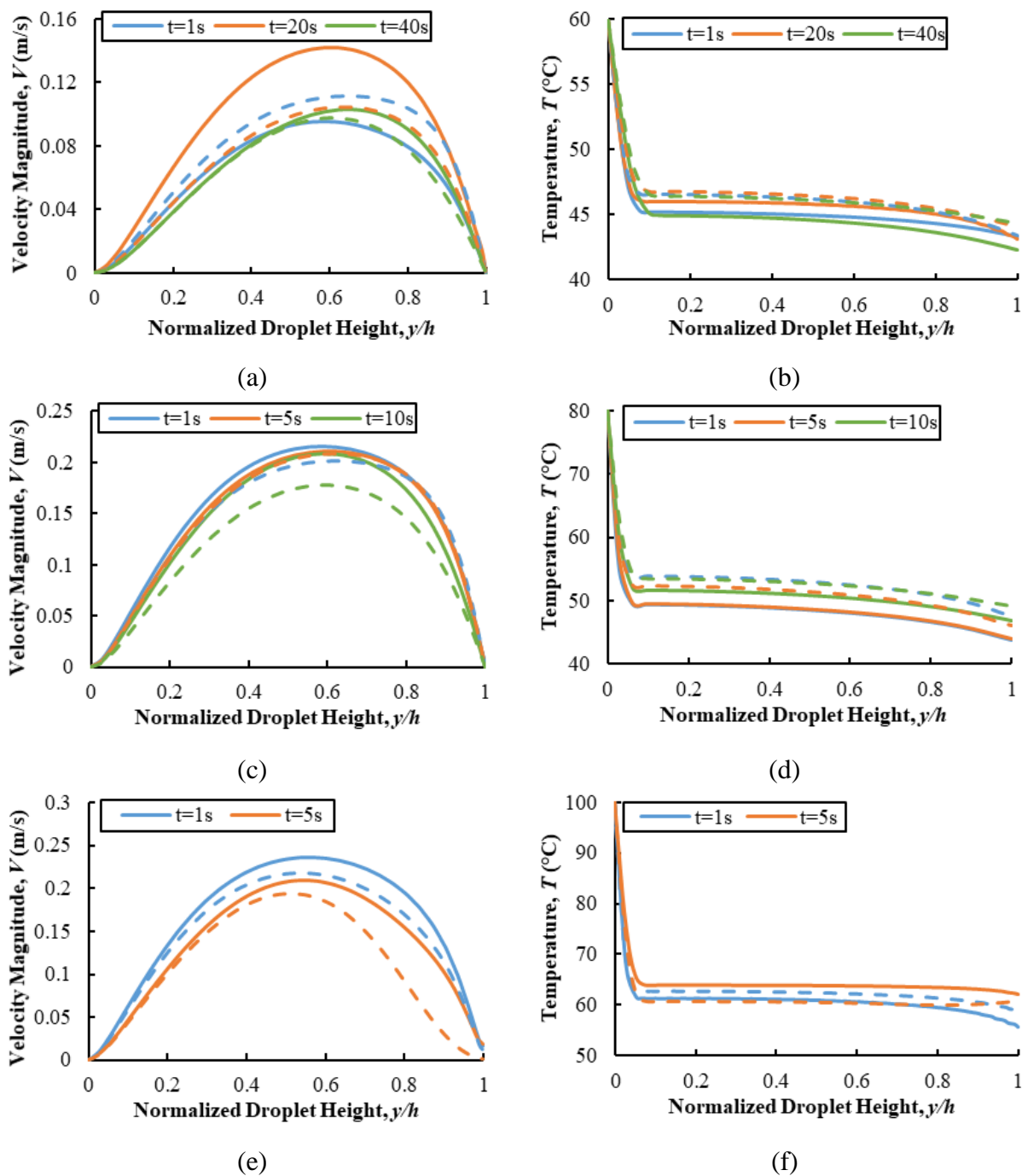
828 Fig. 4 Variation of the Marangoni number with evaporation time of H₂O droplets (black markers) and CAHF droplets (colored
 829 markers) at a copper plate surface temperature of (a) 60 °C, (b) 80 °C and (c) 100 °C.

830

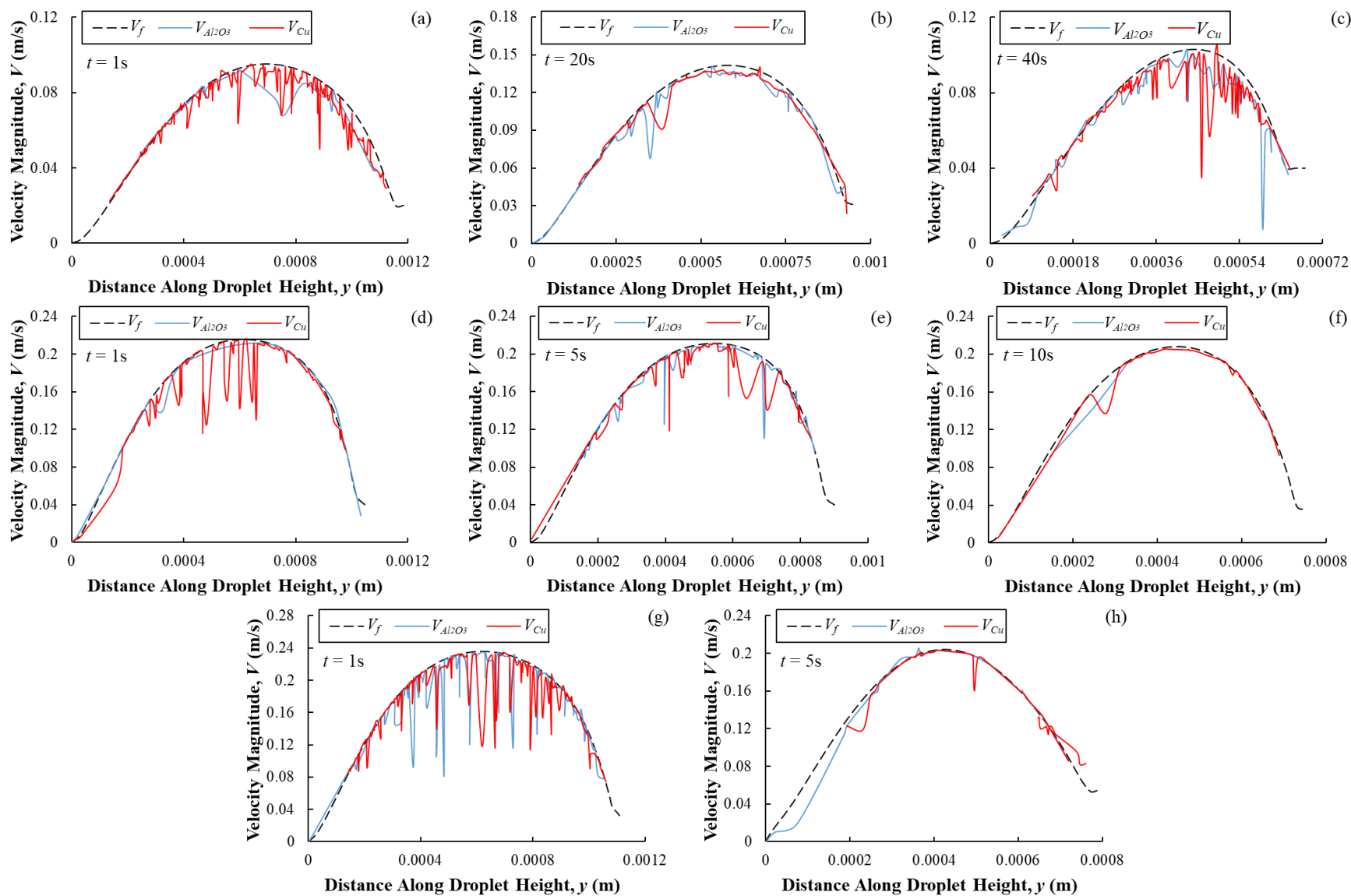


831 Fig. 5 Comparison of (a, c, e) velocity and (b, d, f) temperature fields of 3 μl CAHF (droplet left
 832 half) and H_2O (droplet right half) droplets for different time instants during evaporation at $T_s =$
 833 60°C . Pink and blue suspended particles are copper and alumina nanoparticles, respectively.

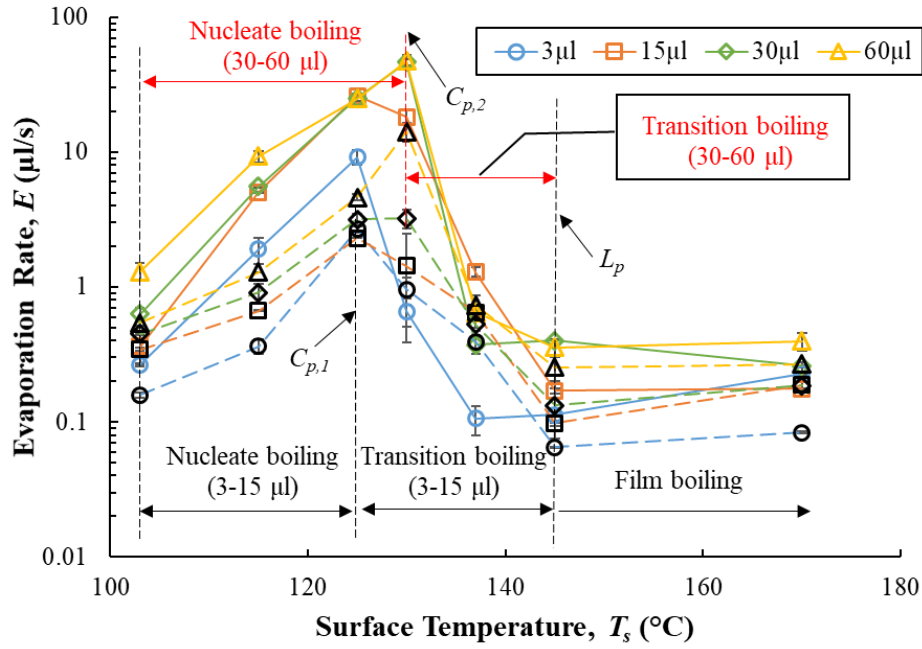
834



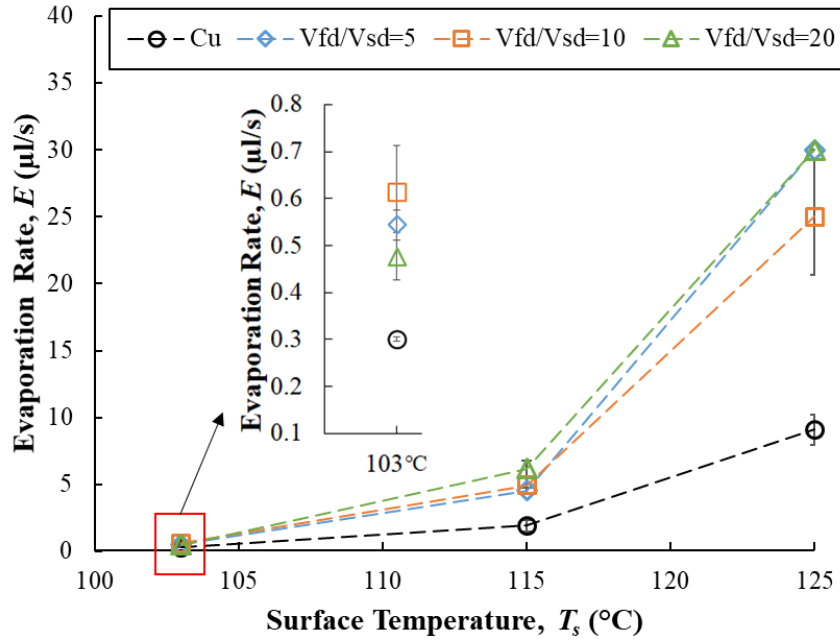
836 Fig. 6 Variation of fluid (a) velocity and (b) temperature profiles along the droplet height inside a
 837 3 μ l droplet at $T_s = 60$ °C. Solid and dashed lines correspond to CAHF and H₂O droplets,
 838 respectively. Plots (c, d) and (e, f) correspond to $T_s = 80$ °C and $T_s = 100$ °C, respectively.



839 Fig. 7 Comparison of fluid velocity (V_f) and hybrid nanoparticles velocity ($V_{Al_2O_3}$ and V_{Cu}) along droplet height (at $r = 0.03R$) during
 840 evaporation of a $3 \mu\text{l}$ volume of CAHF droplet at (a-c) $T_s = 60 \text{ }^\circ\text{C}$, (d-f) $T_s = 80 \text{ }^\circ\text{C}$ and (g, h) $T_s = 100 \text{ }^\circ\text{C}$.



(a)

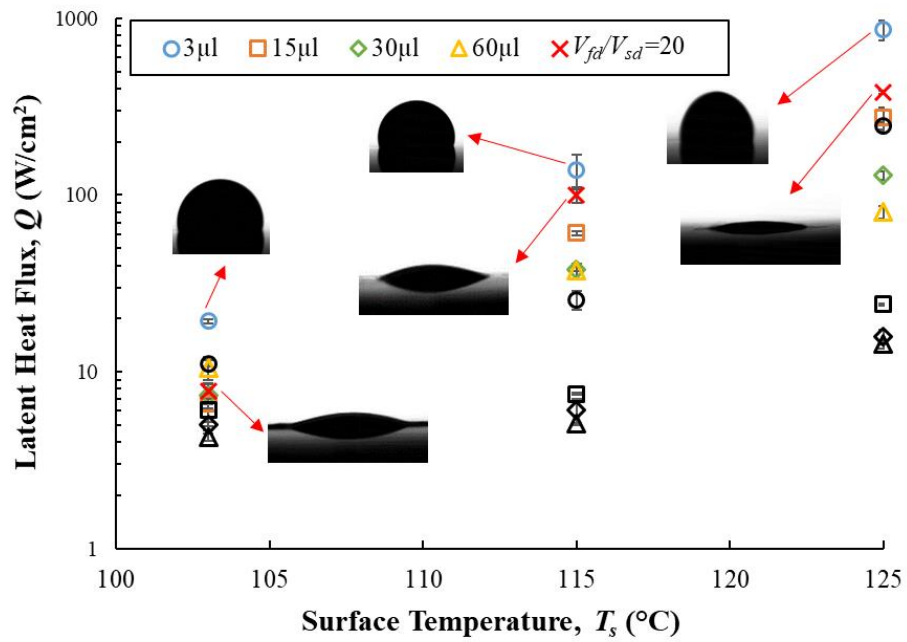


(b)

841 Fig. 8 (a) Evaporation rate of H₂O droplets (black markers, dashed lines) and CAHF droplets
 842 (colored markers, solid lines) in different droplet boiling regimes, (b) evaporation rate of a 3 μl
 843 CAHF droplet on a copper surface (black markers) and residue surfaces (colored markers) in the
 844 nucleate boiling regime.

845

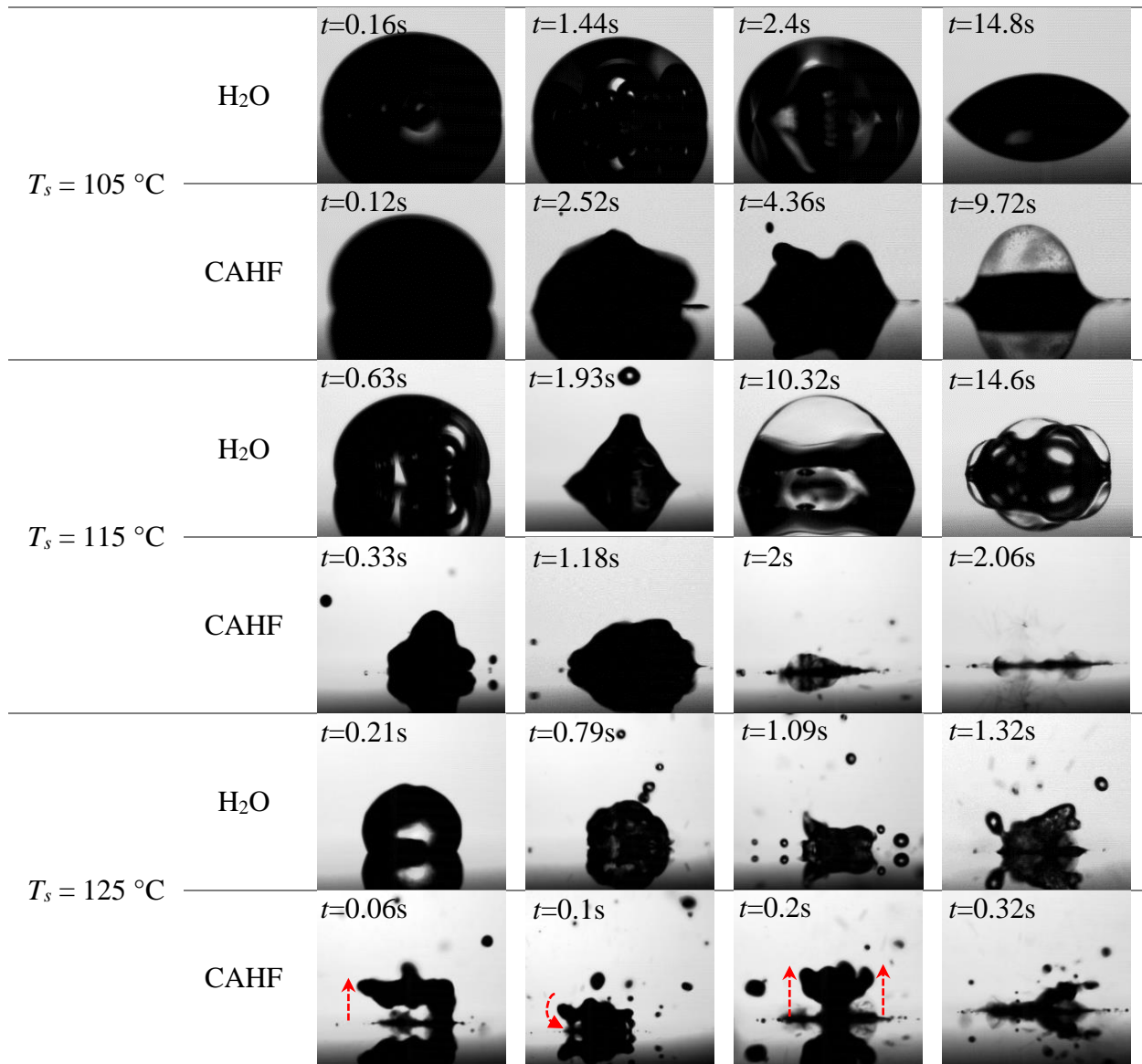
846
847
848
849
850



851
852
853
854
855

Fig. 9 Latent heat flux of water droplets (black markers) over a copper surface and CAHF droplets (colored markers) over copper and residue surfaces ($V_{fd}/V_{sd} = 20$) in the nucleate boiling regime. Insets show 3 µl CAHF droplet over copper and residue surfaces.

856
857



858 Fig. 10 Comparison in boiling dynamics of 15 μl volume of water and CAHF droplets over a
859 heated copper surface in the nucleate boiling regime.
860